https://doi.org/10.5194/egusphere-2026-1411
Preprint. Discussion started: 8 April 2026

Explicit Numerical Simulations of Hailstorm Seeding with a Three–Moment Microphysics Cloud–Resolving Model: A Comparison of Two Operational Methodologies for Hail Suppression

Darko Savić[1], Vladan Vučković[1], Dragana Vujović[1]
[1]University of Belgrade, Faculty of Physics, Belgrade, 11001, Serbia
Correspondence to: Darko Savić (darko.savic@ff.bg.ac.rs)

Abstract.

The global trend of increasing economic losses due to hailstorms sustains the relevance of hail suppression as a weather modification technique. However, quantifying the physical effectiveness of operational cloud seeding remains a significant challenge due to the inherent nonlinearity and complexity of convective processes.

In this study, we use a 3–dimensional numerical model, ARPS (Advanced Regional Prediction System), featuring a three–moment microphysical scheme to simulate the seeding of a supercell. The model is improved by implementing a two–moment aerosol microphysics that accounts for all the known scavenging processes and parameterizations of all four ice–nucleating modes. The prognostic equations for aerosol mixing ratio and number concentration in the air and in each hydrometeor category were calculated. Simulations were conducted at a high spatial resolution (500 m horizontal, 250 m vertical) over a 3–hour evolution period. This approach allows for a very explicit simulation of processes associated with cloud seeding.

Two operational seeding methodologies were investigated, RHSS (Republic Hydrometeorological Service of Serbia, 2023) and AB23 (Abshaev et al., 2023). The results indicate that both strategies effectively reduce hail–induced crop damage. Total hail kinetic energy decreased by 27% (RHSS) and 17.9% (AB23). Notably, the surface area of moderate risk ($KE_{flux} > 100$ J m^{-2}) was reduced by 36.6% and 38.6%, while high–risk areas ($KE_{flux} > 300$ J m^{-2}) saw a significant reduction of 66% and 88%, respectively.

1 Introduction

Clouds are one of the key subsystems of the Earth's atmosphere, playing a significant role in redistributing heat and moisture, as well as shaping radiation and hydrological processes. Their impact extends across spatial scales from local to global and temporal scales from minutes to the climate scale, with the consequences of intense cloud systems being particularly significant for sectors such as agriculture and transport.

The complexity of cloud systems arises from the nonlinear interactions of processes at different scales, primarily synoptic and microphysical. Cloud microphysics is itself extremely complex (Morrison et al., 2020; Khain et al., 2000) and includes processes occurring on scales from approximately 10^{-8} m for aerosol particles (APs) to about 10^{-1} m for hailstones, representing a difference of seven orders of magnitude (Straka, 2009). The inclusion of synoptic processes further expands the range of relevant scales and increases the complexity of their numerical representation.

Cumulonimbus (Cb) clouds are of particular interest because of their association with intense weather events, including downdrafts, hail, electrical discharges, and strong winds. Owing to their pronounced dynamics, microphysical complexity, and significant impacts, these systems are intensively researched in atmospheric sciences. Extreme weather events linked to Cb clouds are among the main reasons for the decades–long scientific effort to improve numerical weather models and forecasting systems for such processes. Warning systems and mechanisms to reduce material damage caused by convective clouds require special attention and are increasingly discussed.

The fact that the Central Balkan region is identified as one of the regions with the most favourable conditions for the formation of Cb clouds in Europe (Brooks et al., 2003) further supports research on these phenomena. Since the pioneering works of Schaefer (1946) and Vonnegut (1947), many scientific projects (American Society of Civil Engineers, 2015; Dessens et al., 2016; Rauber et al., 2019) and operational programs (American Society of Civil Engineers, 2015; Dessens et al., 2016) have employed cloud seeding technology worldwide to either enhance precipitation or suppress hail. Silver iodide (AgI) is the most widely used glaciogenic seeding material (DeMott, 1995; Marcolli et al., 2016). However, evaluating the effectiveness of cloud seeding has proved to be a very difficult task. Several studies have provided evidence supporting hail mitigation through cloud seeding, using different delivery technologies, including ground–based generators (Dessens et al., 2016), rockets (Mesinger and Mesinger, 1992; Simeonov, 1996; Vujović et al, 2007), and aircraft (Rudolf et al., 1994; Smith et al., 1997).

The development and increasing availability of computational resources, along with recent knowledge advancements in microphysics and numerical techniques (Loftus, 2012), have made numerical models indispensable tools for understanding the chain of events of physical processes associated with cloud seeding practices (American Society of Civil Engineers, 2015; Rauber et al., 2019; Garstang et al., 2005). Numerical models have enabled explicit analysis of the influence of seeding materials on microphysical processes in clouds very explicitly, and allowed sensitivity studies for both idealized (Xue et al., 2013a) and realistic scenarios (Xue et al., 2013b). This approach can also be used to evaluate the effectiveness of a particular weather modification technique or a new seeding material (Lompar et al., 2018), even before physical experiments are conducted.

Hailfall characteristics are determined by the microphysical properties of the cloud and its dynamical structure. The accuracy of numerically simulated hailstorms depends largely on the microphysical scheme used. While bulk numerical models can reproduce most hailstorm features, three–moment microphysical schemes generally yield improved results compared to one and two–moment schemes (Loftus, 2012; Milbrandt and Yau, 2005a; 2005b; 2006a; 2006b).

Vučković (2003) incorporated a reagent seeding scheme into ARPS and conducted numerical cloud seeding experiments, varying the amount of injected reagent, seeding method, and reagent activity. All seeding experiments resulted in increased total rainfall. He concluded that the amount of hail decreased in some areas and increased in others, due to changes in the

https://doi.org/10.5194/egusphere-2026-1411
Preprint. Discussion started: 8 April 2026

width of the seeding zone and the amount of added reagent. The seeding influenced the dynamic processes within the cloud, as shown by intensified vertical movements.

Previous research based on numerical simulations of dispersion and microphysical responses of convective systems using three–dimensional mesoscale numerical models has shown that the efficiency of cloud seeding is strongly dependent on the cloud's dynamics and reagent dispersion (Ćurić et al., 2006; 2007). In addition, Kovačević (2019, 2023) highlighted the importance of the physical and chemical properties of aerosols, indicating that hail suppression is influenced by the characteristics of environmental cloud condensation nuclei (CCN), including their size distribution and solubility in water. Research conducted by Ćurić et al. (2008, 2009) suggests that cloud seeding affects precipitation not only within the target area but also leads to significant spatial redistribution and inadvertent weather modification through the advection and diffusion of unused reagents. These findings highlight the complexity of seeding material transport beyond the intended boundaries, which can result in secondary precipitation maxima and unintended meteorological effects in downwind regions. More recent studies (Papaevangelou et al., 2025; 2026) extended this framework by applying selective seeding of naturally occurring thunderstorms and using ensemble modeling across multiple cases to examine the range of microphysical responses to seeding. Their findings, however, indicate an ambiguous impact of seeding on hail characteristics.

Furthermore, physical experiments on cloud seeding are actively being conducted as a novel approach to verify parameterizations implemented in numerical models (Omanovic et al., 2024). For an objective assessment of hail–induced crop damage, Ursu et al. (2025) introduced an innovative approach of identifying a swath with a high probability of crop damage by relating satellite–derived NDVI (Normalized Difference Vegetation Index) to hail kinetic energy flux. Their results are very useful for evaluating the effectiveness of numerical models of cloud seeding.

The approach proposed in this paper is distinguished by a highly explicit treatment of aerosols with ice nucleation abilities, a feature lacking in the previously mentioned research employing numerical models.

2 Methods

Evaluating the effects of cloud seeding has always been a significant challenge for researchers, particularly when seeding convective clouds. These types of clouds are characterised by small spatial and temporal scales and considerable variability. Additionally, hail precipitation further increases this variability, making it demanding to estimate the effects of seeding on hail suppression, which is the focus of this paper. Due to these hailstorm characteristics, it is difficult to statistically retrieve a microphysical signal of seeding.

For this reason, we used a numerical model to simulate the hail–producing supercell cloud in order to evaluate hail suppression practices for two different operational approaches. Current computational resources allow us to simulate the physical processes involved in cloud seeding explicitly. Therefore, using numerical models, it is possible to track the complete chain of events, from the injection of aerosol particles (APs) into the seeding zone, to AP scavenging by hydrometeors, followed by nucleation, and finally their redistribution among different hydrometeor categories and their washout by precipitation. By employing this method and comparing the control with the seeding experiment, differences in microphysical processes can be identified, as well as changes in hail characteristics within the cloud and at the ground.

2.1 Model Setup

For this study, we used a 3D cloud–resolving numerical model, ARPS (Advanced Regional Prediction System), version 5.3.4 (Xue et al., 2000; 2001), with three–moment microphysics. The numerical model is freely available and developed by the Center for Analysis and Prediction of Storms at the University of Oklahoma. The microphysics scheme (Milbrandt and Yau, 2005a) includes six hydrometeor categories: two liquid (cloud droplets and raindrops) and four solid (cloud ice, snow, graupel, and hail).

The model is upgraded with a two–moment aerosol scheme described in detail in Vučković et al. (2022). In this parameterisation, APs are represented by a gamma distribution with prognostic equations for the mixing ratio and total number concentration of APs in the air and in each hydrometeor category. Furthermore, all known aerosol scavenging processes are included in the model (Table 1). The parameterization, along with the effects of scavenging processes on aerosol particles injected into the convective cloud, is discussed in detail by Vučković et al. (2023; 2025a; 2025b). For all experiments, the intensity of cloud electrification is set to $\alpha = 3$ ($\alpha \in [0, 7]$), corresponding to a moderately charged cumulonimbus cloud. In the model, it is assumed that APs can serve as ice nuclei (IN); therefore, the characteristics such as activity and density of aerosols in the model match those of silver iodide (AgI), because it is used as a seeding reagent whose number size distribution and activity are described in the works by Meyers et al. (1995) and DeMott (1982; 1995), respectively. It is also important to note that the model's coordinate system was moving at 3 m s^{-1} due east and 14 m s^{-1} due north to account for the storm's relatively large velocity and to keep it near the center of the domain.

The domain of integration covers a volume of 120 × 120 × 17.5 km^3, with a horizontal resolution of 500 m and a vertical resolution of 250 m. The integration used a large time step of 2 s and a small time step of 0.5 s, with the simulated period covering 3 hours of cloud evolution. The domain had rigid wall conditions at the top and bottom and open lateral boundaries. The model employs a 1.5–order TKE closure coupled with the Moeng–Wyngaard subgrid–scale turbulence scheme (Moeng and Wyngaard, 1989). Scalar advection is handled by the multidimensional Zalesak flux–corrected transport method (Zalesak, 1979). The hailstorm is initiated with a 4 K potential temperature perturbation in the form of an ellipsoidal bubble in a horizontally homogeneous environment characterized by radio–sounding data. The sounding describes the conditions of an unstable atmosphere with strong vertical wind shear, which favours the development of organized convection. The sounding is well known in the literature and will be examined in detail in Sect. 3.1.

Table 1. Aerosol scavenging processes implemented in the ARPS model within the two–moment microphysics scheme

Cloud Droplets	Raindrops	Cloud Ice	Snow	Graupel
Brownian diffusion	Brownian diffusion	Brownian diffusion	Brownian/turbulent diffusion	Brownian diffusion
Thermophoresis	Thermophoresis	Thermophoresis	Thermophoresis	Thermophoresis
Diffusiophoresis	Diffusiophoresis	Diffusiophoresis	Diffusiophoresis	Diffusiophoresis
Turbulent diffusion	Directional interception	Electroscavenging (Coulomb)	Directional interception	Directional interception
Electroscavenging (Coulomb + image charge)	Electroscavenging (Coulomb)		Electroscavenging (Coulomb)	Electroscavenging (Coulomb)

2.2 Operational Cloud Seeding

According to the World Meteorological Organization statement on weather modification (WMO, 2025), more than 50 countries use some form of weather modification, usually seeding with nucleating aerosol particles, to disperse fog, enhance precipitation, or mitigate hail. Many countries have operational practices of convective cloud seeding with glaciogenic material to suppress hail–induced damage. These seeding methodologies usually rely on beneficial competition by using glaciogenic APs and in this research, we investigated two methodologies that have been in use for several decades.

2.2.1 Republic Hydrometeorological Service of Serbia Methodology

Serbia has employed cloud seeding for hail mitigation for almost 60 years (since 1967) under the supervision of the Republic Hydrometeorological Service of Serbia; this methodology will therefore be referred to as RHSS in the following text. The full procedure for hail suppression using this methodology is described in the Republic Hydrometeorological Service of Serbia (2023). The Hail Suppression Center of Serbia operates for six months each year, from 15 April to 15 October, using rocket technology to deliver the seeding material to the clouds.

The RHSS methodology is based on the detection of four variables derived from radar data, as presented in Table 2.

Table 2. RHSS methodology criteria for cloud seeding

	Symbol	Variable	Radar reflectivity value	Criterion for seeding
1.	H_{ct}	cloud top maximum height	15 dBZ	$H_{ct} \geq H$ (T = −28 °C)
2.	H_{ez}	enhanced radar reflectivity zone maximum height	45 dBZ	$H_{ez} \geq H$ (T = −14 °C)
3.	H_{Zmax}	maximum reflectivity height	/	$H_{Zmax} \geq H$ (T = 0 °C)
4.	Zmax	maximum reflectivity	/	Zmax ≥ 45 dBZ

The height of characteristic isotherms from Table 2 is obtained from a numerical weather model or sounding data. When RHSS criteria are observed by a radar operator (except for the fourth criterion in the case of a developing cell, described below), the first phase of cloud seeding is initiated, determining the type of convective process. RHSS recognises five types of convective processes:

1. Developing cell,
2. Single cell axisymmetric stationary process,
3. Single cell nonsymmetric moving process,
4. Multicell process, and
5. Supercell process

After determining the type of convective process, the seeding zone is identified. It is located in the vicinity of the hail embryo formation zone (EFZ) and includes a part of it. In the RHSS methodology, rockets are aimed at −6 ± 3 °C, effectively covering the vertical range from 0 °C to −10 °C. In the model, the upper and lower boundaries are set as the 0 °C and −10 °C isotherms, respectively. Horizontally, these zones are confined between 45 dBZ and 15 dBZ (hatched red in Fig. 1), except for the Developing cells (type 1), which are seeded over the entire area of 15 dBZ. As previously mentioned, the seeding zone should include part of the EFZ and is located near the main updraft (Young, 1993; Abshaev et al., 2014; 2023). For Single cell axisymmetric stationary processes (type 2), the EFZ is located symmetrically around the updraft in a volume resembling a torus. In contrast, moving clouds (types 3–5) are characterized by the EFZ, that is usually located on the cloud's periphery in front of the main updraft axis. After identifying the seeding zone, the reagent mass is calculated based on the horizontal surface area of the zone using lookup tables developed by RHSS. This mass is evenly distributed within the seeding zone volume in the numerical model. If a Developing cell is identified, one seeding cycle is used. For types 2–5, the number of seeding cycles depends on the maximum radar reflectivity as follows:

- 45 dBZ ≤ Zmax < 55 dBZ → 2 seeding cycles
- 55 dBZ ≤ Zmax < 65 dBZ → 3 seeding cycles
- Zmax ≥ 65 dBZ → at least 4 seeding cycles

Seeding cycles are separated by 5–minute time intervals. If any of the criteria from Table 2 cease to be valid, seeding is terminated for the next 5 minutes when the criteria checking is resumed.

2.2.2 Methodology of Abshaev et al. (2023)

The seeding methodology proposed by Abshaev et al. (2014; 2023, denoted AB23) is presented in this section. The first step is to determine the type of convective process, or the "seeding object" (SO), as defined by Abshaev et al. (2023). This methodology recognises four seeding objects, from SO_I, the weakest type of storm, to SO_{IV}, the most severe. The AB23 methodology uses a significantly more complex set of criteria for SO type categorisation compared to RHSS. Table 3 lists the thresholds for the different SOs. The definitions of the variables in Table 3 are as follows:

- Zmax → radar reflectivity maximum (in dBZ)
- ΔH_x → height of the radar reflectivity (in km) of x dBZ measured above the 0 °C isotherm, where x ∈ [Zmax, 35, 45]
- Δq_m → vertically integrated water content (VIL) maximum (in kg m^{-2}) above the 0 °C isotherm
- ΔM_x → integrated water content within the x dBZ reflectivity volume (in ton) above the 0 °C isotherm, where x ∈ [25, 35, 45, 55]

Table 3. AB23 methodology criteria for cloud seeding

	Criteria thresholds					
SO_I	$0 < \Delta H_{Zmax} < 5$	$15 < Zmax < 45$	$\Delta q_m \geq 0.5$	$\Delta M_{25} > 10$	$\frac{d\Delta q_m}{dt} > 0$	$d\Delta M_{25} > 0$
SO_{II}	$\Delta H_{35} > 3$	$Zmax \geq 45$	$\Delta q_m \geq 2$	$\Delta M_{35} > 2 \cdot 10^4$	$\frac{d\Delta q_m}{dt} > 0$	$d\Delta M_{35} > 0$
SO_{III}	$\Delta H_{45} \geq 3$	$Zmax \geq 55$	$\Delta q_m > 8$	$\Delta M_{45} > 2 \cdot 10^4$	/	/
SO_{IV}	$\Delta H_{45} > 4$	$Zmax > 65$	$\Delta q_m > 16$	$\Delta M_{55} > 2 \cdot 10^5$	/	/

As stated in Abshaev et al. (2023), seeding is usually performed at the level of −6 ± 3 °C. Therefore, in the model, seeding is carried out between 0 °C and −10 °C, facilitating comparison between different experiments. SO_I is seeded over the entire area with 15 dBZ reflectivity. The SO_{II} seeding zone is horizontally bounded by the 35 dBZ reflectivity and the border of the radar echo (1 dBZ in the model), which is indicated by hatched green lines in Fig. 1. The SO_{III} and SO_{IV} seeding zones are also horizontally bounded by the 35 dBZ reflectivity on one side and by a line extending 5 km beyond the radar echo boundary into the cloud–free region on the other side (1 dBZ + 5 km into the cloud–free region in the model). This zone is shown in Fig. 1 as green dots. Regarding the seeding cycles:

- SO_I → 1seeding cycle
- SO_{II} → 2 seeding cycles
- SO_{III} (weak and moderate) → 3 seeding cycle (every 7 min)
- SO_{III} (intense) and SO_{IV} → 4 seeding cycle (every 3.5 min)

For practical reasons, the model was set up in a way that $\mathrm{SO_{III}}$ was seeded 3 times and $\mathrm{SO_{IV}}$ 4 times, every 7 minutes. An important thing to mention is that, although Abshaev et al. (2023) report the initial number concentration of the seeding material for effective hail prevention should be $N_{\mathrm{Tap}} \geq 10^{11}$ $\mathrm{m^{-3}}$, to have comparable total masses of APs injected in experiments of both methodologies, we used $N_{\mathrm{Tap}} = 10^{8}$ $\mathrm{m^{-3}}$ for AB23.

Examining the RHSS and AB23 methodologies reveals that the main differences between them are the seeding criteria, the seeding zones (Fig. 1), and the seeding cycle time intervals. Three experiments were conducted in this study: a control experiment (CTRL) without seeding, and one for each methodology described earlier (RHSS and AB23).

The simulated supercell exhibited a somewhat anomalous motion, moving due north (Sect. 3.1). In the northern hemisphere, supercells typically move eastward and have inflow located south of them (Fig. 1). In the model, the seeding zone is defined as follows. First, the location of the maximum updraft is identified, and a vector originating from that point and directed along the x–axis is constructed. Second, grid boxes within a specified reflectivity and temperature range are searched within a 120° sector to the right of this vector (clockwise), indicated by orange arrows in Fig. 1. To limit seeding in parts of the cloud far from the EFZ, seeding is permitted within 10 km of the location of the maximum updraft.

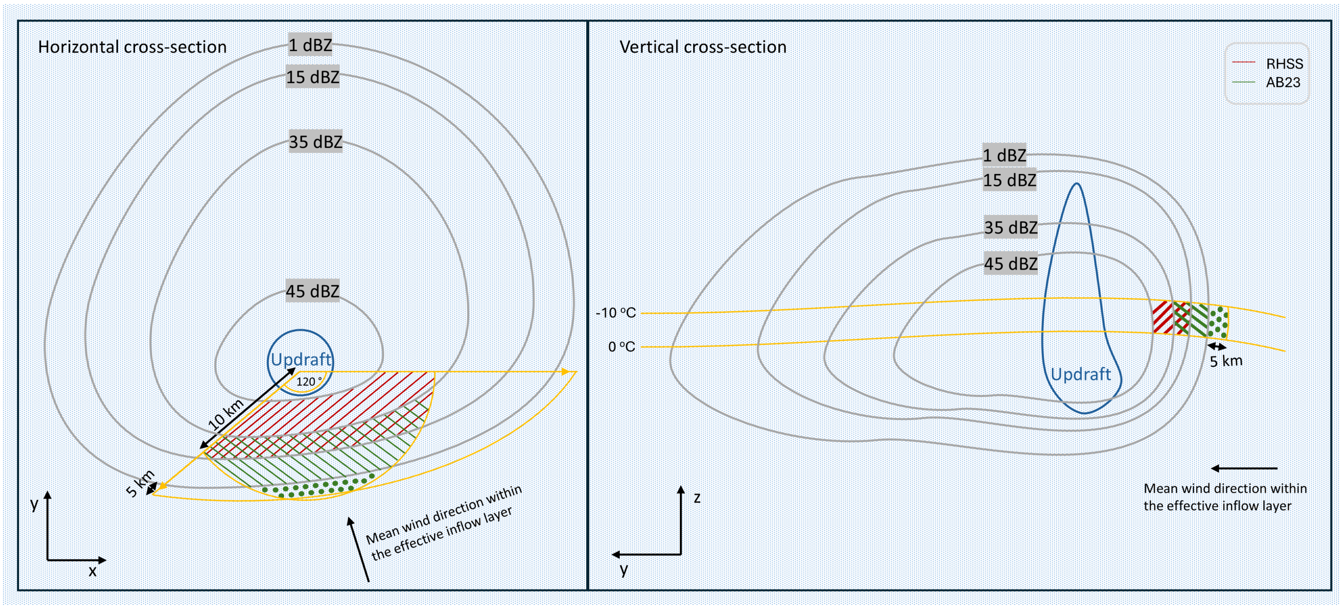

Figure 1. Scheme of the seeding zone for the RHSS (red) and AB23 (green) methodologies. The left panel shows the horizontal cross–section, while the right panel shows the vertical cross–section. Note that this scheme does not apply to RHSS type 1 and 2 processes, nor to the $\mathrm{SO_{I}}$ process in AB23.

https://doi.org/10.5194/egusphere-2026-1411
Preprint. Discussion started: 8 April 2026

3 Results

3.1 Environmental Drivers for Hailstorm Formation

As mentioned previously, the hailstorm was initiated in the numerical model ARPS using radio–sounding data. The Skew–T diagram is shown in Fig. 2. Radio–sounding data indicate very unstable environmental conditions, with a Surface–Based Convective Available Potential Energy (SBCAPE) of 3381 J kg^{-1} and no Convective Inhibition (CIN). This, combined with a relatively low Lifting Condensation Level (LCL) and Level of Free Convection (LFC), both close to 730 m ASL, is conducive to deep convection. High surface moisture at the surface is indicated by a high surface dew point temperature of approximately 21 °C. The clockwise hodograph shows strong vertical wind shear, indicating favourable conditions for organized convection, specifically a right–moving supercell cloud. This supercell is estimated to be moving north–northeast at around 30 knots, as indicated by the arrow.

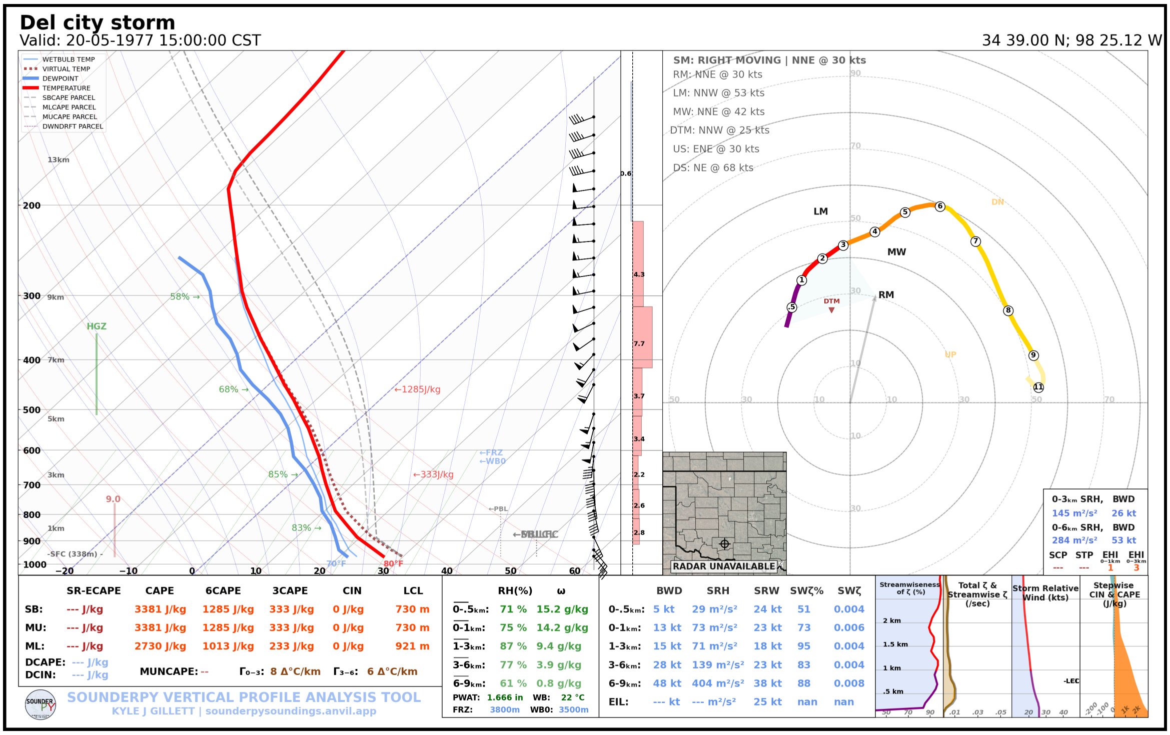

	SR-ECAPE	CAPE	6CAPE	3CAPE	CIN	LCL
SB:	--- J/kg	3381 J/kg	1285 J/kg	333 J/kg	0 J/kg	730 m
MU:	--- J/kg	3381 J/kg	1285 J/kg	333 J/kg	0 J/kg	730 m
ML:	--- J/kg	2730 J/kg	1013 J/kg	233 J/kg	0 J/kg	921 m

DCAPE: --- J/kg
DCIN: --- J/kg
MUNCAPE: --
Γ_{0-3}: 8 Δ°C/km
Γ_{3-6}: 6 Δ°C/km

	RH(%)	ω
$\overline{0\text{-}.5}_{km}$:	71 %	15.2 g/kg
$\overline{0\text{-}1}_{km}$:	75 %	14.2 g/kg
$\overline{1\text{-}3}_{km}$:	87 %	9.4 g/kg
$\overline{3\text{-}6}_{km}$:	77 %	3.9 g/kg
$\overline{6\text{-}9}_{km}$:	61 %	0.8 g/kg

PWAT: 1.666 in WB: 22 °C
FRZ: 3800m WB0: 3500m

	BWD	SRH	SRW	SWζ%	SWζ
$0\text{-}.5_{km}$:	5 kt	29 m²/s²	24 kt	51	0.004
$0\text{-}1_{km}$:	13 kt	73 m²/s²	23 kt	73	0.006
$1\text{-}3_{km}$:	15 kt	71 m²/s²	18 kt	95	0.004
$3\text{-}6_{km}$:	28 kt	139 m²/s²	23 kt	83	0.004
$6\text{-}9_{km}$:	48 kt	404 m²/s²	38 kt	88	0.008
EIL:	--- kt	--- m²/s²	25 kt	nan	nan

$0\text{-}3_{km}$ SRH,	BWD
145 m²/s²	26 kt

$0\text{-}6_{km}$ SRH,	BWD
284 m²/s²	53 kt

SCP	STP	EHI $_{0-1km}$	EHI $_{0-3km}$
---	---	1	3

Figure 2. Skew–T sounding of "Del city storm" for May 20, 1977. 21.00 UTC (16.00 local time). Python library SounderPy (Gillet, 2025) was used to make this figure. Environmental temperature (red line) and dew point temperature (blue line) are on the left panel. Hodograph with estimated velocity and direction of the right–moving cell is on the right panel. Below, various convective indices are calculated along with moisture and vorticity variables.

The sounding we used is well known and thoroughly researched in the scientific literature. This data relates to a synoptic situation in which sixteen storms (Ray et al., 1981) occurred during the afternoon and evening hours of 20 May and the early morning hours of 21 May 1977. The storm, which also produced a tornado, formed at about 1600 (CST) and was named the "Del city storm". The supercell developed rapidly, exhibiting a characteristic low–level mesocyclone and a hook radar echo prior to tornadogenesis (Brandes, 1981; Klemp and Rotunno, 1983). The observed storm features were also successfully reproduced using numerical models (Klemp et al., 1981; Noda and Niino, 2003).

245 In our numerical simulations, the storm took about 40 minutes to split into a left–moving cell, which quickly weakened and left the domain, and a right–moving supercell. The evolution of the storm, in the CTRL experiment, examined through radar reflectivity at 2 km height, is shown in Fig. 3. The updraft is indicated by a red isoline of vertical velocity threshold of 5 m s^{-1}. Only the right–moving supercell was seeded.

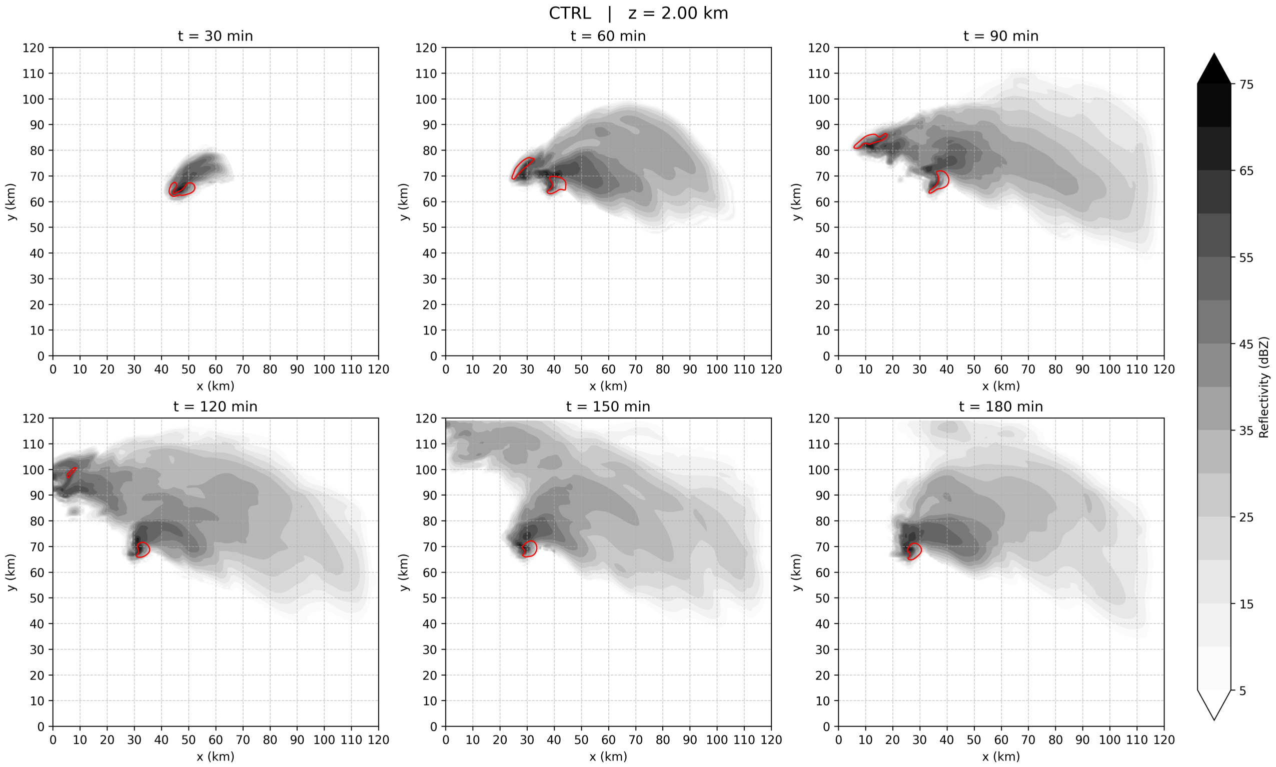

250

Figure 3. Supercell evolution presented by the radar reflectivity (grey color) for the CTRL experiment, given every 30 minutes at a height of 2 km. The updraft threshold of 5 m s^{-1} is marked by a red isoline.

3.2 Microphysical Responses to Cloud Seeding

255 The approach described in Sect. 2.1 enables explicit tracking of aerosol fate within the model. Both AP number concentration and mixing ratios have their prognostic equations for the air and for each hydrometeor category in this two–moment AP microphysics scheme. This allows investigation of all the physical processes to which the injected particles

are exposed in every grid box, from the rate of their removal from the atmosphere by hydrometeors, to their activation as IN in cloud droplets and raindrops, and eventually their redistribution among different hydrometeor categories due to microphysical interactions.

The total mass of injected reagent (cyan lines in Fig. 4) is comparable for both methodologies throughout the entire 3 h period, although for AB23, a larger amount of seeding material is injected about 40% more. For AB23, the total mass is approximately 70 kg, and for RHSS, 50 kg. It should be noted that after about the 1 h mark, part of the cloud's anvil begins to leave the domain; therefore, a small fraction of cloud ice and aerosols are lost due to advection through the sides of the domain. In Fig. 4, it can be seen that the seeding criteria for AB23 are met a few minutes earlier than for RHSS.

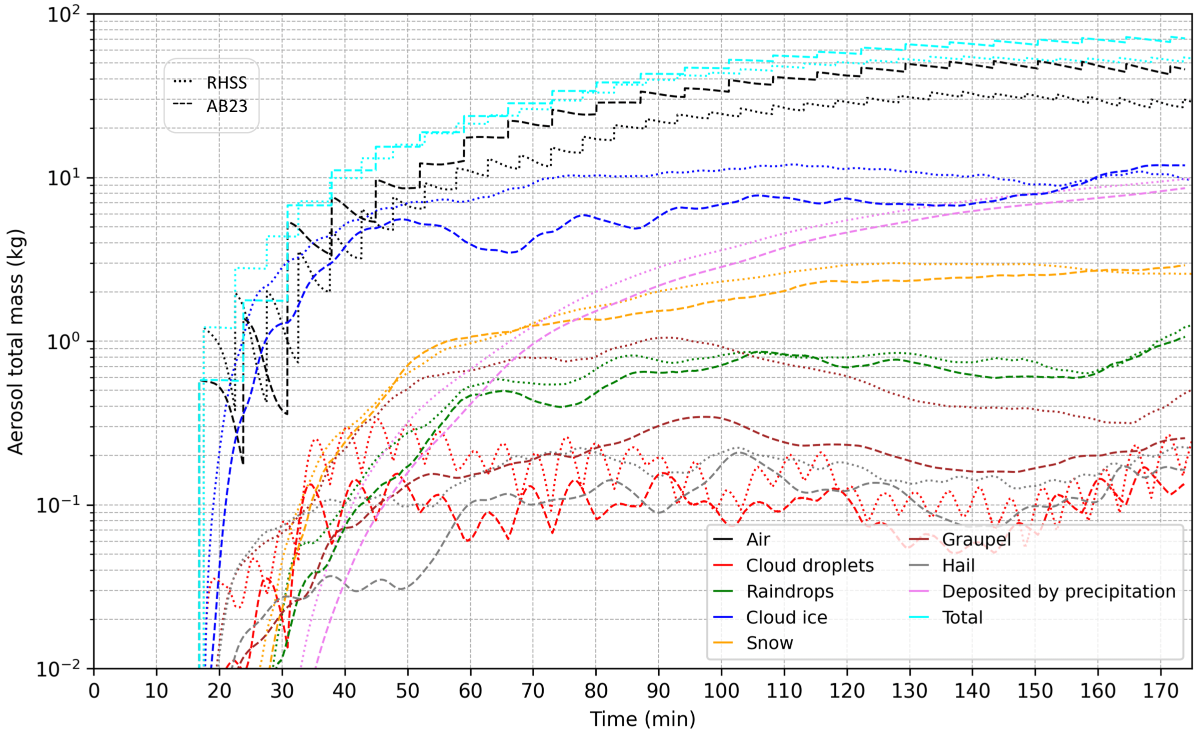

Figure 4. The time series of aerosol total mass in the air and in each hydrometeor category for the entire model domain. The case of RHSS methodology is depicted with dotted lines, and for AB23 with dashed lines.

The strongest signal as a response to cloud seeding, as expected, is observed in cloud droplets (red lines). Each individual seeding cycle is clearly visible in both methods as a sudden increase in AP mass in cloud droplets due to scavenging, followed by a decrease caused by activation as INs. It is also evident that, for RHSS, there is more AP mass in cloud droplets, especially during the first 2 hours, which can be attributed to differences in the seeding zones. In the case of AB23, the seeding material is also dispersed in front of or outside the cloud; therefore, it takes some time for the reagent material to be advected into the volume containing supercooled droplets, scavenged from the air, and ultimately nucleate as ice particles. As a result of intentionally seeding the supercooled part of the cloud, most of the AP mass ends up in cloud ice (blue lines). Although the RHSS methodology delivered less seeding material, it contains more AP mass in cloud ice for about 2.5 hours of integration, after which AB23 prevails. This may also be explained by a slower and steadier supply of ice–nucleating particles to the zone of supercooled liquid.

Aerosol total mass in graupel shows the greatest difference when comparing the two methodologies, with more APs are contained in graupel in the case of RHSS throughout the integration period. Furthermore, the total mass of APs deposited on the surface by precipitation increased steadily, reaching about 10 kg at the end of the integration period, although slightly more AP mass was deposited in the case of RHSS.

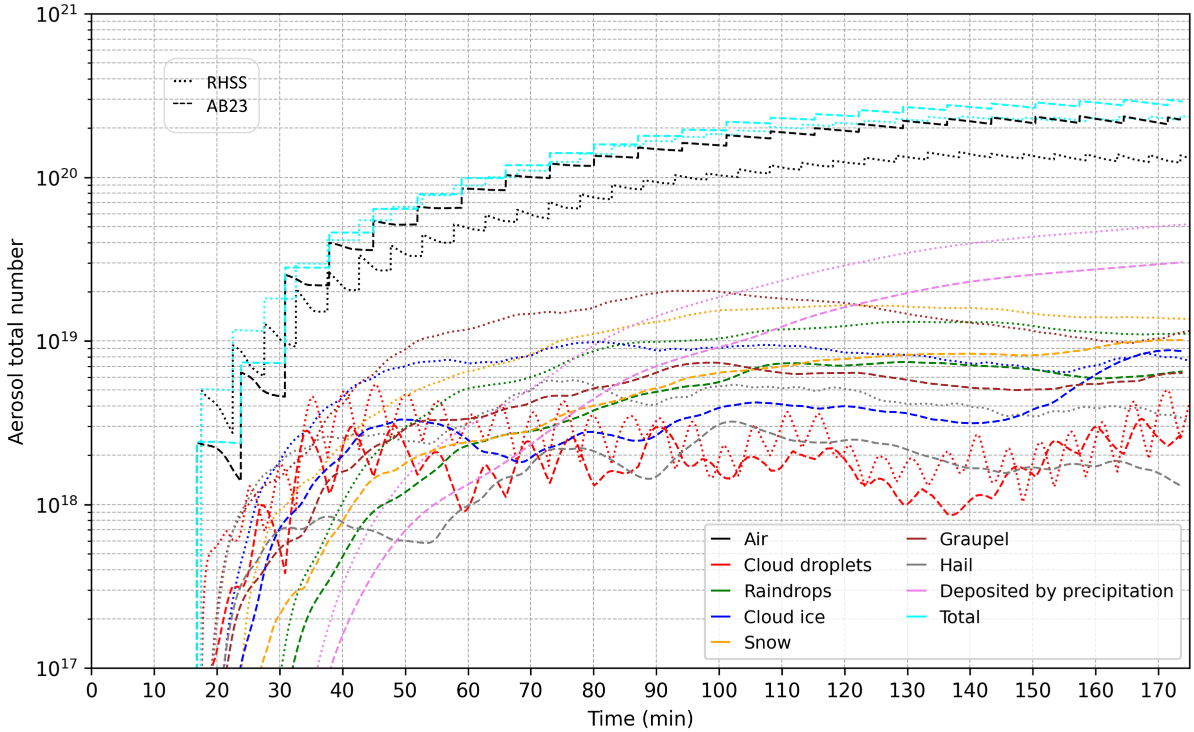

Figure 5. The time series of aerosol total number in the air and in each hydrometeor category for the entire model domain. The case of RHSS methodology is depicted with dotted lines, and for AB23 with dashed lines.

Examining the total AP number (Fig. 5), a similar conclusion is reached, with some key differences. First, there is a greater difference in the total AP number across hydrometeor categories between these two methodologies. Second, cloud ice is not the dominant AP reservoir in terms of number, compared to mass (Fig. 4). Finally, most APs scavenged, in terms of their number, are washed out by precipitation. All these differences can be attributed to the use of a non–monodisperse aerosol distribution. According to the dependence of AP scavenging on particle diameter (Vučković et al., 2022, 2023, 2025a, 2025b), where smaller particles are collected more efficiently by hydrometeors, the difference between the two cases is explained by the slower collection of small APs by hydrometeors in AB23, due to the seeding zone being partially outside the cloud, which affects particle number more than mass. Conversely, smaller ice–nucleating particles are less active than larger ones; that is, i.e., smaller APs, which contribute more to the number than to the mass of collected particles, are activated as IN to a lesser extent, and thus fewer of them are transferred from cloud droplets to cloud ice after nucleation.

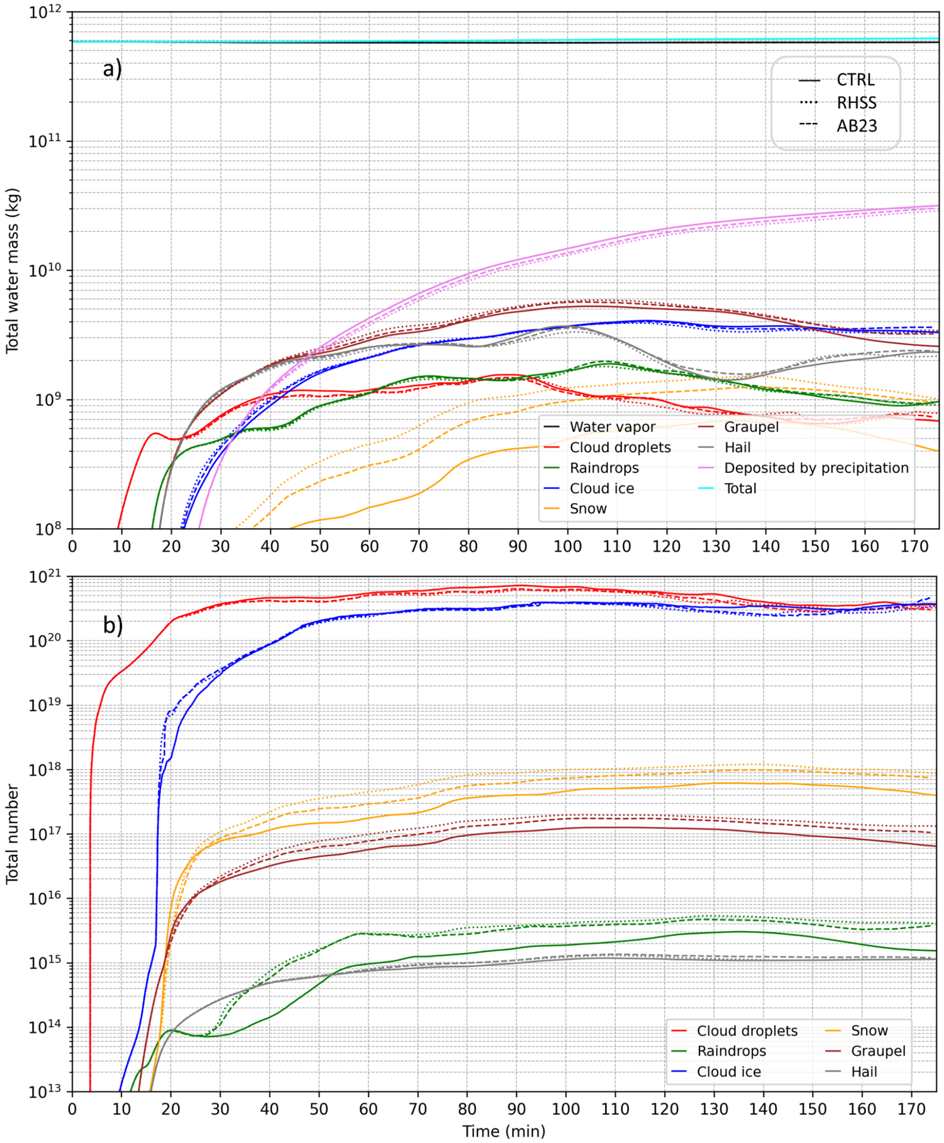

Figure 6. The time series of the total mass **(a)** and number of particles **(b)** in each hydrometeor category for the entire model domain. The CTRL case is depicted with a solid line, the RHSS methodology with dotted lines, and AB23 with dashed lines.

The effects of seeding the cloud with glaciogenic material on the total mass and number of hydrometeors in the model domain are shown in Fig. 6 a) and b), respectively. As both seeding methodologies have almost the same effect on increasing or decreasing specific microphysical processes, and due to the large number of figures, the results of the RHSS method will be compared to CTRL and examined in this section. The corresponding figures for the AB23 methodology can be found and are available for interpretation in Appendix A.

To understand the seeding signal, it is useful to examine the individual microphysical processes within each hydrometeor category and compare the CTRL and seeding cases. This approach enables a detailed understanding of the processes involved in cloud seeding. In Sect. 3.2.1–3.2.6, we will thoroughly investigate the microphysical response to seeding for cloud droplets, raindrops, cloud ice, snow, graupel, and hail, respectively.

3.2.1 Cloud droplets response

Targeting the zone of hail embryo formation, supercooled cloud droplets are the first to respond to the injected reagent. Figure 7 shows the microphysical source and sink terms for cloud droplet mass in the CTRL experiment (a) and RHSS (b). In the seeding case, the most noticeable sinks are those related to contact and immersion freezing of cloud droplets on AgI particles (red and light red in Fig. 7b, respectively). Both freezing processes are of the same order of magnitude in this case, although immersion freezing displays a very distinct step–like seeding cycle signal, in contrast to contact freezing. This behaviour is explained by the freezing mechanism itself. When APs are injected into the seeding zone, they are collected by the cloud droplets. As soon as they reach the nucleation temperature for immersion freezing, they activate as immersion INs; hence, the step–like trend is observed. In contrast, contact freezing, in addition to being a function of temperature, also depends on the AP collection rate (Table 1), which is why the line is flatter in Fig. 7b.

Freezing of cloud droplets, which introduces more ice particles into the seeding zone, also affects accretion processes. This is evident from the increased riming of ice crystals, snow, and graupel (blue, light blue, and orange lines in Fig. 7, respectively). All these effects combined result in a decrease in the total mass of cloud droplets for the first 130 minutes (red lines, Fig. 6a). The conversion of small raindrops to cloud droplets is also increased due to seeding, indicating a reduction in raindrop size, but this process is negligible.

Similar conclusions can be drawn by investigating the source and sink terms for the number of cloud droplets (Fig. 8). The most visible difference is in contact freezing (red line in Fig. 8b), which shows a sharper response to seeding cycles compared to the mass of cloud droplets. This can be partially explained by the fact that more numerous, small droplets collect APs more efficiently, making the number of droplets more sensitive to this mechanism. This may seem paradoxical, considering that collection is proportional to droplet size and thus contact freezing, but a large number of small drops may dominate AP collection. This also coincides with the decrease in the number of droplets in Fig. 6b (red lines).

https://doi.org/10.5194/egusphere-2026-1411
Preprint. Discussion started: 8 April 2026

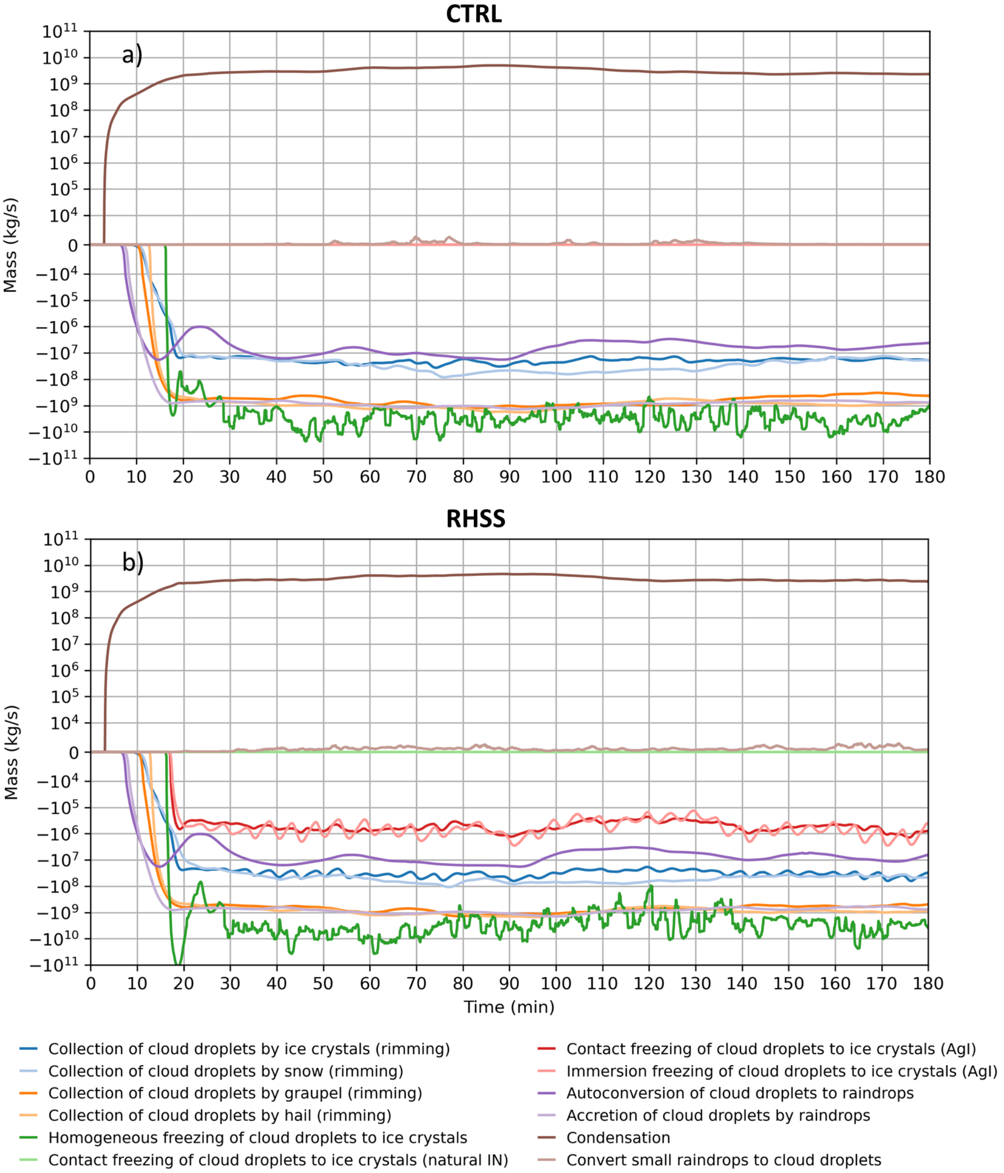

Figure 7. The time series of source/sink terms for the cloud droplet total mass in the domain for CTRL **(a)** and RHSS **(b)** cases. Different microphysical processes are depicted with different colors indicated in the figure's legend at the bottom. The values of the quantities are averaged over 1 minute.

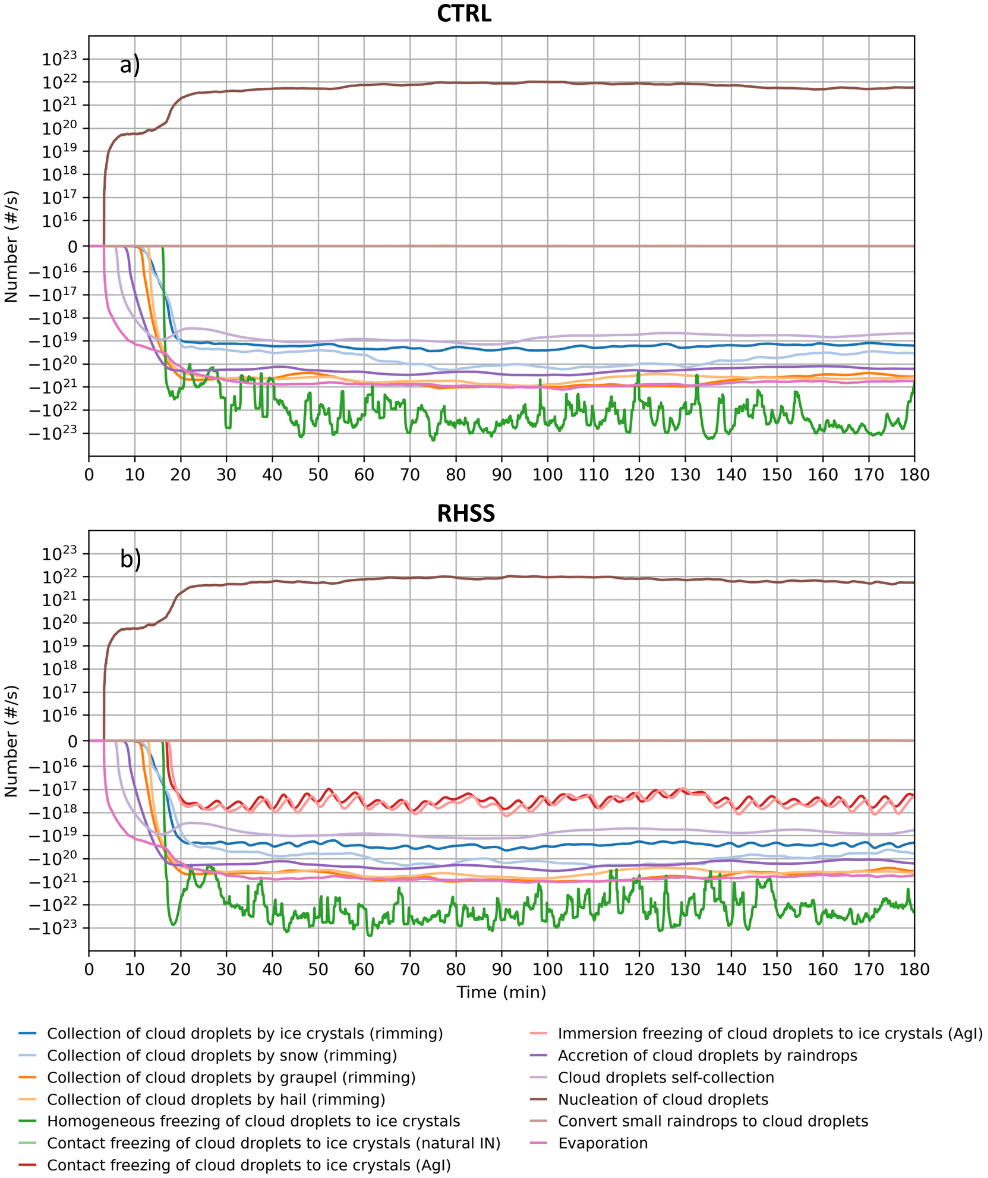

Figure 8. The time series of source/sink terms for the cloud droplet total number in the domain for CTRL **(a)** and RHSS **(b)** cases. Different microphysical processes are depicted with different colors indicated in the figure's legend at the bottom. The values of the quantities are averaged over 1 minute.

3.2.2 Raindrops response

Raindrops are also present in the seeding zone, alongside droplets, and they collect APs, which can activate as INs. Raindrops have a mass comparable to that of cloud droplets (Fig. 6a) but are much less numerous (Fig. 6b). This difference is evident when we examine the source and sink terms for the mass of raindrops (Fig. 9). Immersion freezing of raindrops (brown line in Fig. 9b) becomes a significant sink process, showing a similar step–like trend as for droplets. In contrast, the

https://doi.org/10.5194/egusphere-2026-1411
Preprint. Discussion started: 8 April 2026

effect of contact freezing on the mass of raindrops is negligible (light purple in Fig. 9b). Regarding sources, a significant increase is observed for the melting of snow and ice crystals (light blue and purple in Fig. 9, respectively) due to seeding. The effects of seeding are much more pronounced on the total number of raindrops (Fig. 6b) than on their mass (Fig. 6a). Immersion and contact freezing contribute similarly to the number of raindrops (brown and light purple lines in Fig. 10b), with immersion freezing being more dominant. The increase in the total number (Fig. 6b) can be attributed to a net increase in the melting of snow, graupel, and ice crystals (light blue, green, and purple lines in Fig. 10, respectively).

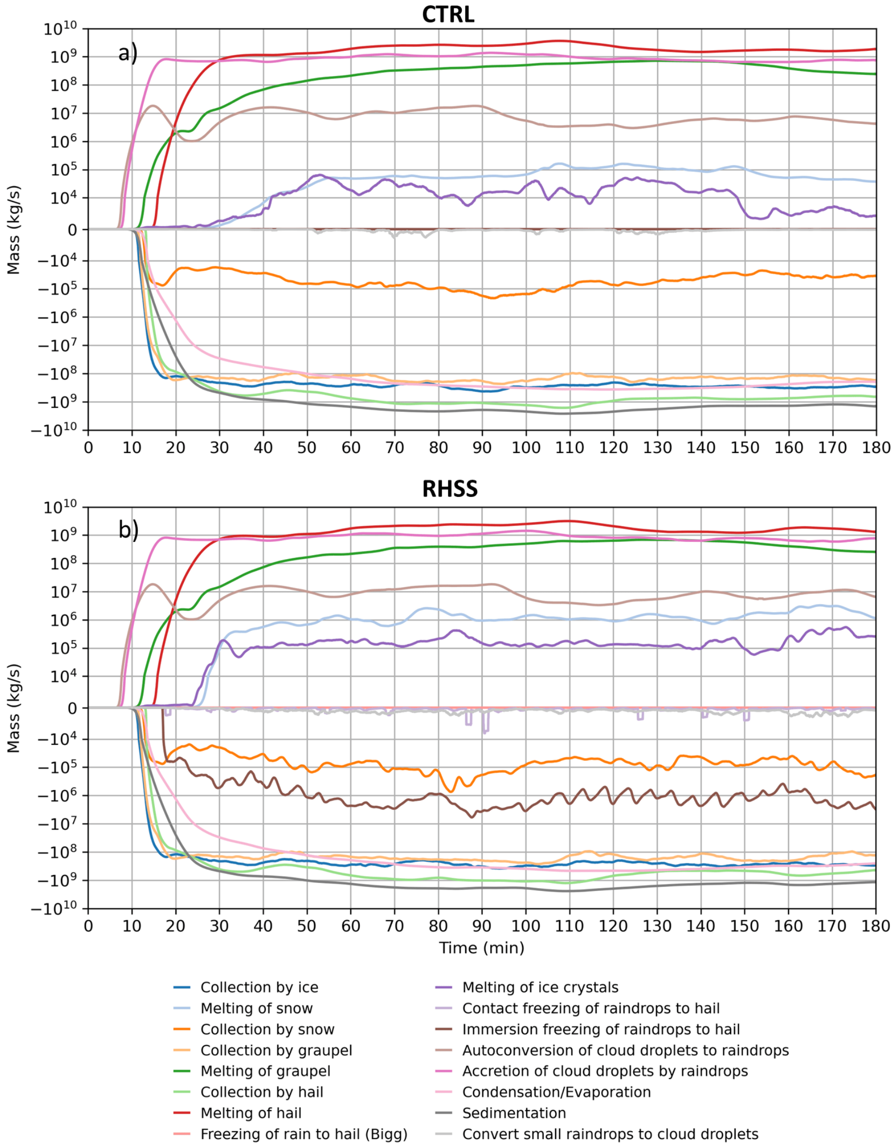

Figure 9. The time series of source/sink terms for the raindrops total mass in the domain for CTRL **(a)** and RHSS **(b)** cases. Different microphysical processes are depicted with different colors indicated in the figure's legend at the bottom. The values of the quantities are averaged over 1 minute.

https://doi.org/10.5194/egusphere-2026-1411
Preprint. Discussion started: 8 April 2026

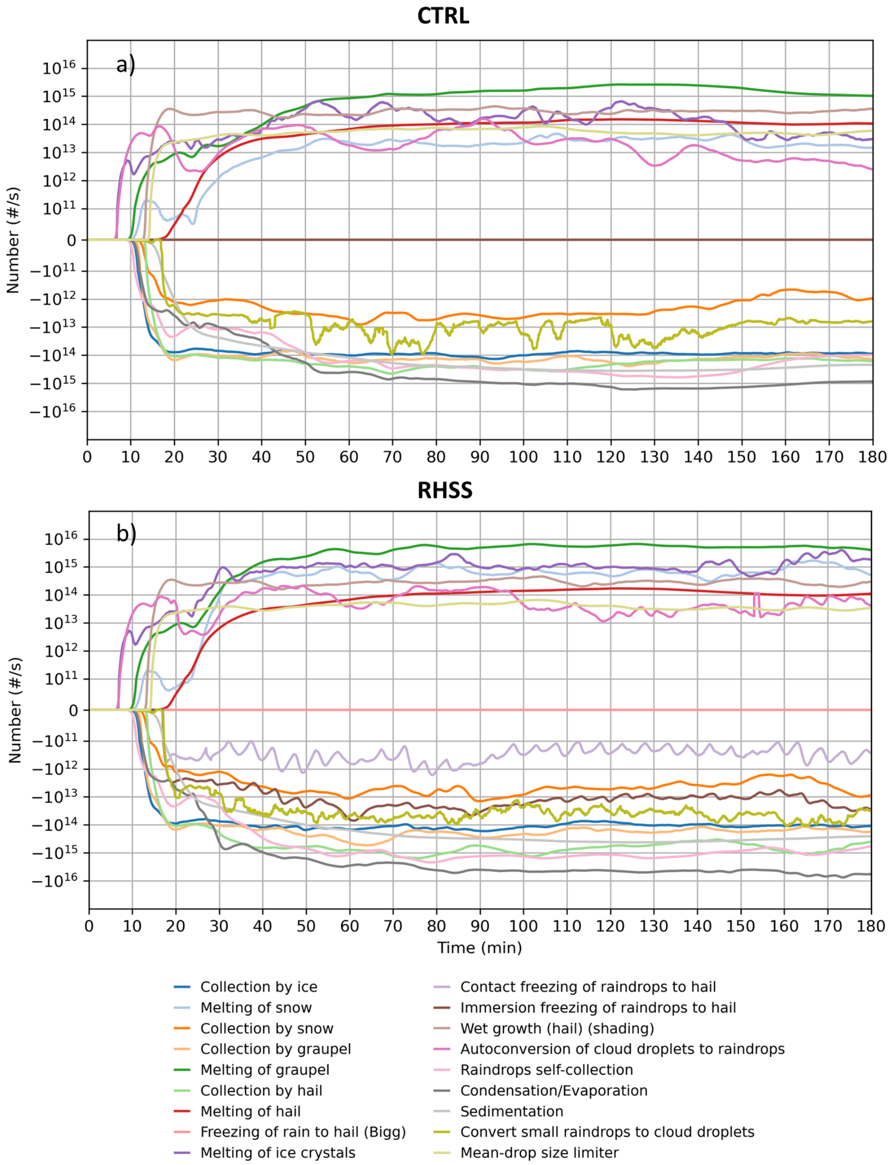

Figure 10. The time series of source/sink terms for the raindrops total number in the domain for CTRL **(a)** and RHSS **(b)** cases. Different microphysical processes are depicted with different colors indicated in the figure's legend at the bottom. The values of the quantities are averaged over 1 minute.

3.2.3 Cloud ice response

The presence of APs had no significant effect on the total cloud ice mass and number (Fig. 6), except for a brief period at the beginning of seeding, from 20 to 30 minutes, and around the 2.5–hour mark. Depositional nucleation, contact freezing, and immersion freezing on AgI particles had the most pronounced effect on cloud ice mass (light blue, olive, and light olive lines in Fig. 11b, respectively) and show comparable values. These processes lead to an increase in cloud ice riming (green line in

Fig. 11). In contrast, the collection of ice crystals by graupel and the conversion of ice to graupel and snow also increased significantly (brown, light green, and light red lines in Fig. 11, respectively). Sorption is negligible as a source of ice crystal mass (orange line in Fig. 11) but does affect ice crystal number (orange line in Fig. 12). However, it remains less significant than the other three nucleation modes.

The effects of seeding with glaciogenic material on cloud ice also appear to be balanced for ice particle number (Fig. 12), and therefore do not significantly change the total number in the domain (Fig. 6b).

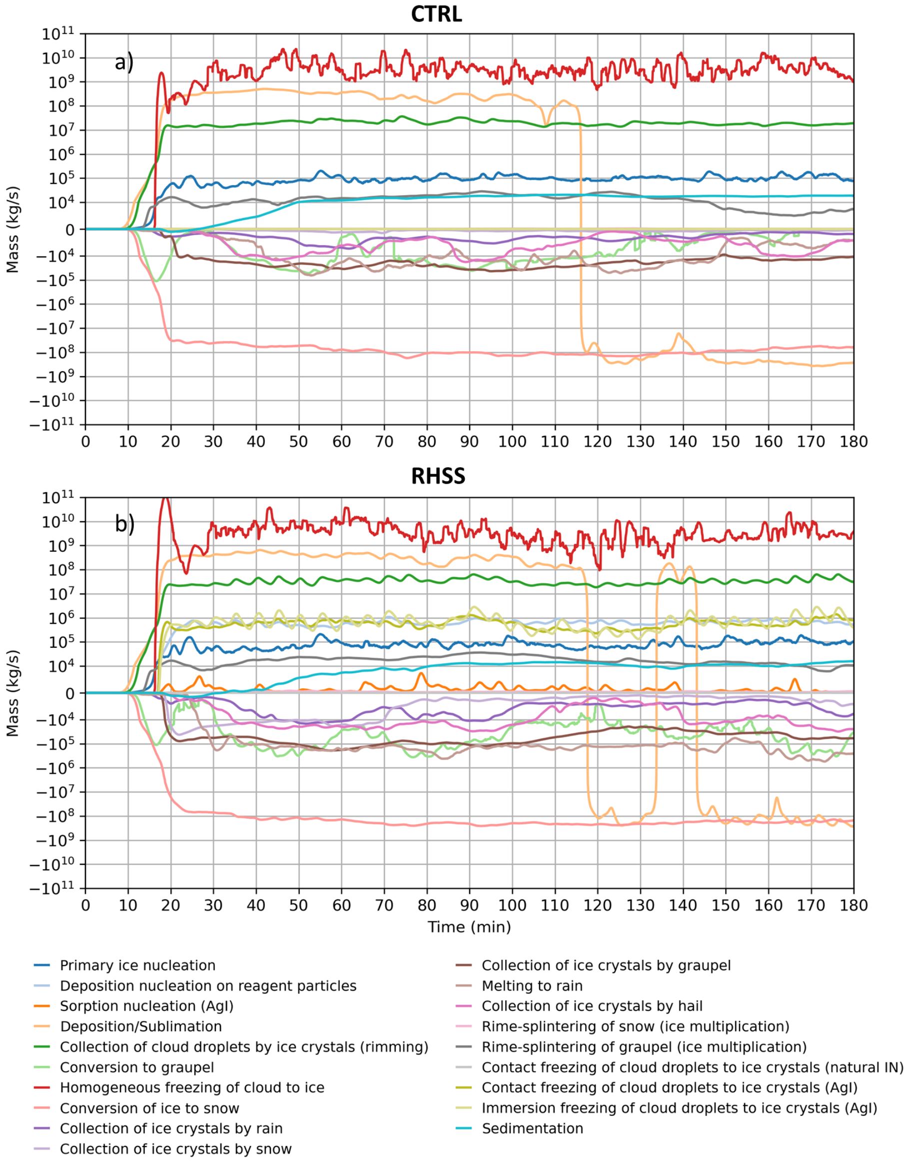

Figure 11. The time series of source/sink terms for the cloud ice total mass in the domain for CTRL **(a)** and RHSS **(b)** cases. Different microphysical processes are depicted with different colors indicated in the figure's legend at the bottom. The values of the quantities are averaged over 1 minute.

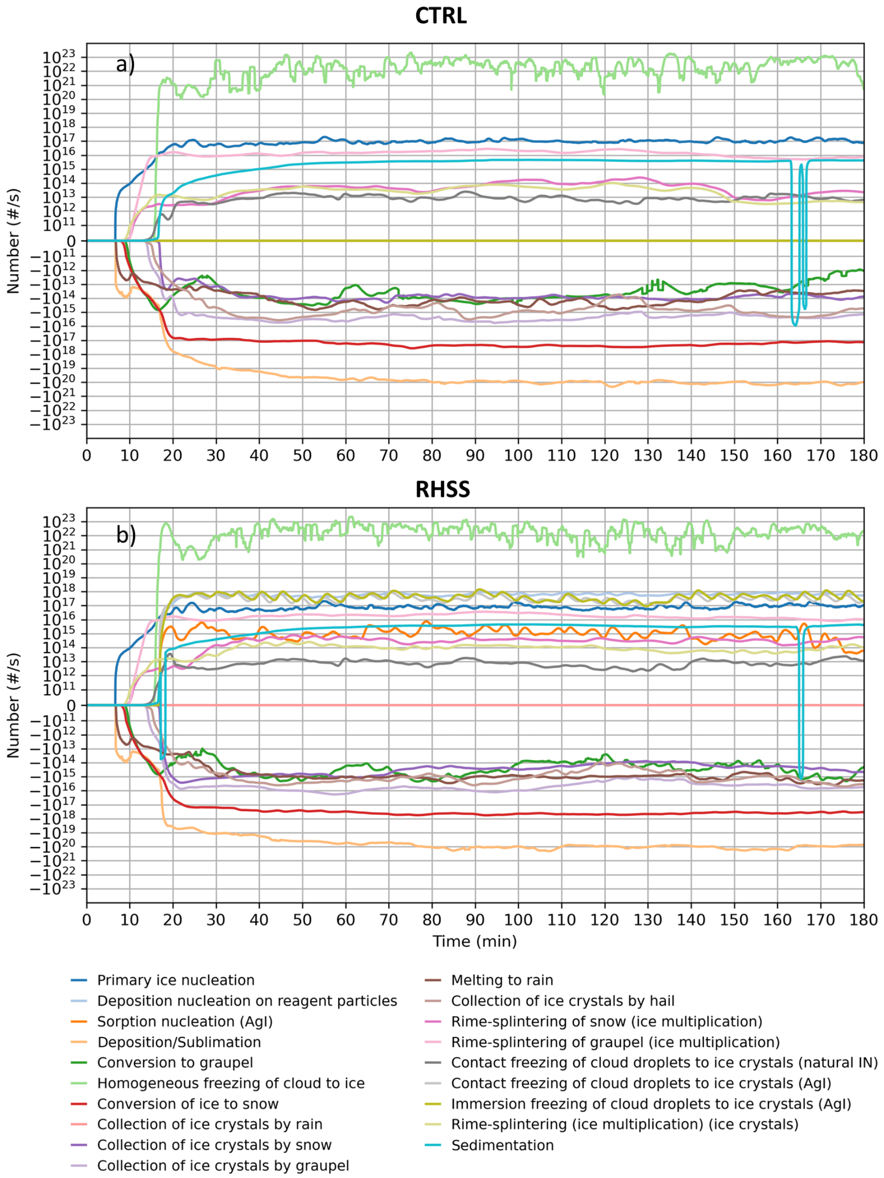

Figure 12. The time series of source/sink terms for the cloud ice total number in the domain for CTRL **(a)** and RHSS **(b)** cases. Different microphysical processes are depicted with different colors indicated in the figure's legend at the bottom. The values of the quantities are averaged over 1 minute.

3.2.4 Snow response

Snow responds most significantly to injected AgI particles in both total mass and number (Fig. 6), compared to other hydrometeors. Seeding increases the total mass and number within the domain throughout the entire integration period. Snow exhibits a more complex response with regard to seeding than hydrometeor categories previously investigated. The largest increases in source terms for snow mass are due to the collection of ice crystals by snow and 3–component freezing

(light red and light purple lines in Fig. 13, respectively). Three–component freezing refers to the interaction of three particle categories in cloud microphysics, where two categories combine to produce particles in a third category. The most important factors contributing to the increase in total snow mass are the higher conversion of ice to snow and snow riming (blue and orange lines in Fig. 13, respectively). Sink terms have also increased, particularly the melting of snow to rain (green line in
390 Fig. 13), as well as the collection of snow by rain and sedimentation (red and brown lines in Fig. 13, respectively).

As a result of a higher number of ice crystals, increased conversion of ice to snow (blue line in Fig. 14) leads to a higher total number of snow particles (Fig. 6b). Conversely, an increased number of snow particles further enhances snow aggregation (light red in Fig. 14).

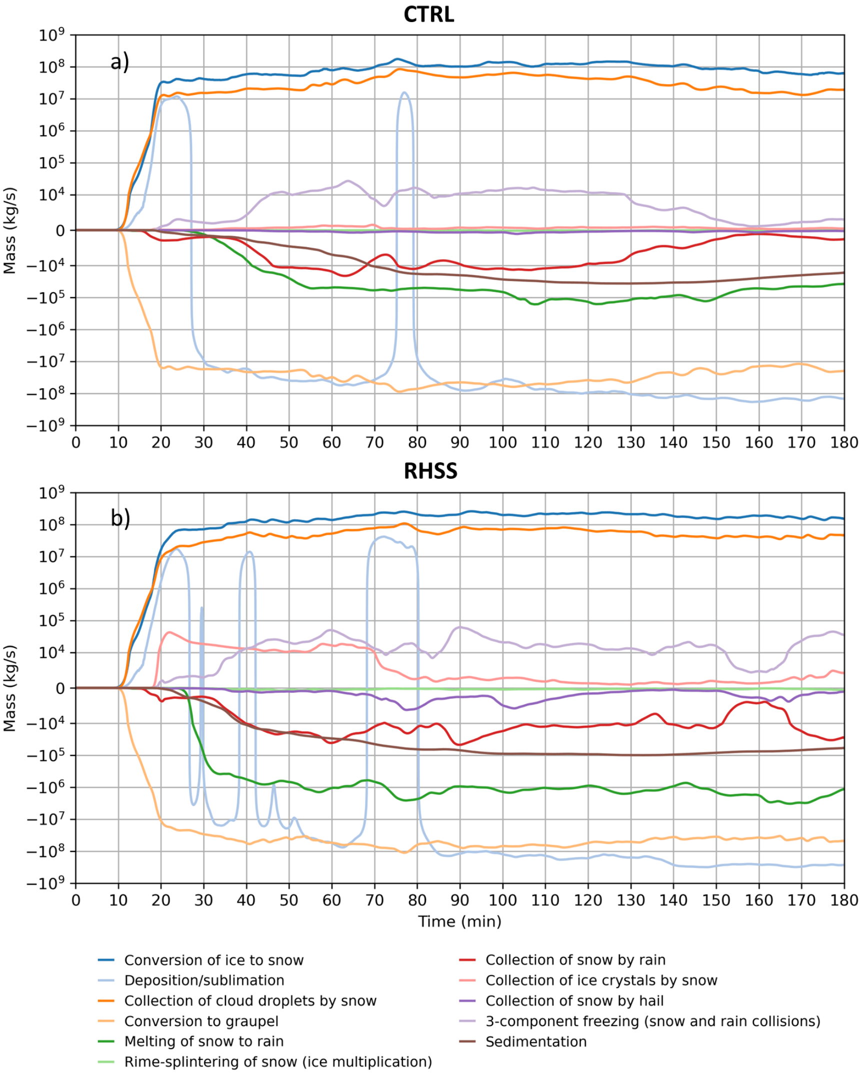

395 **Figure 13.** The time series of source/sink terms for the snow total mass in the domain for CTRL **(a)** and RHSS **(b)** cases. Different microphysical processes are depicted with different colors indicated in the figure's legend at the bottom. The values of the quantities are averaged over 1 minute.

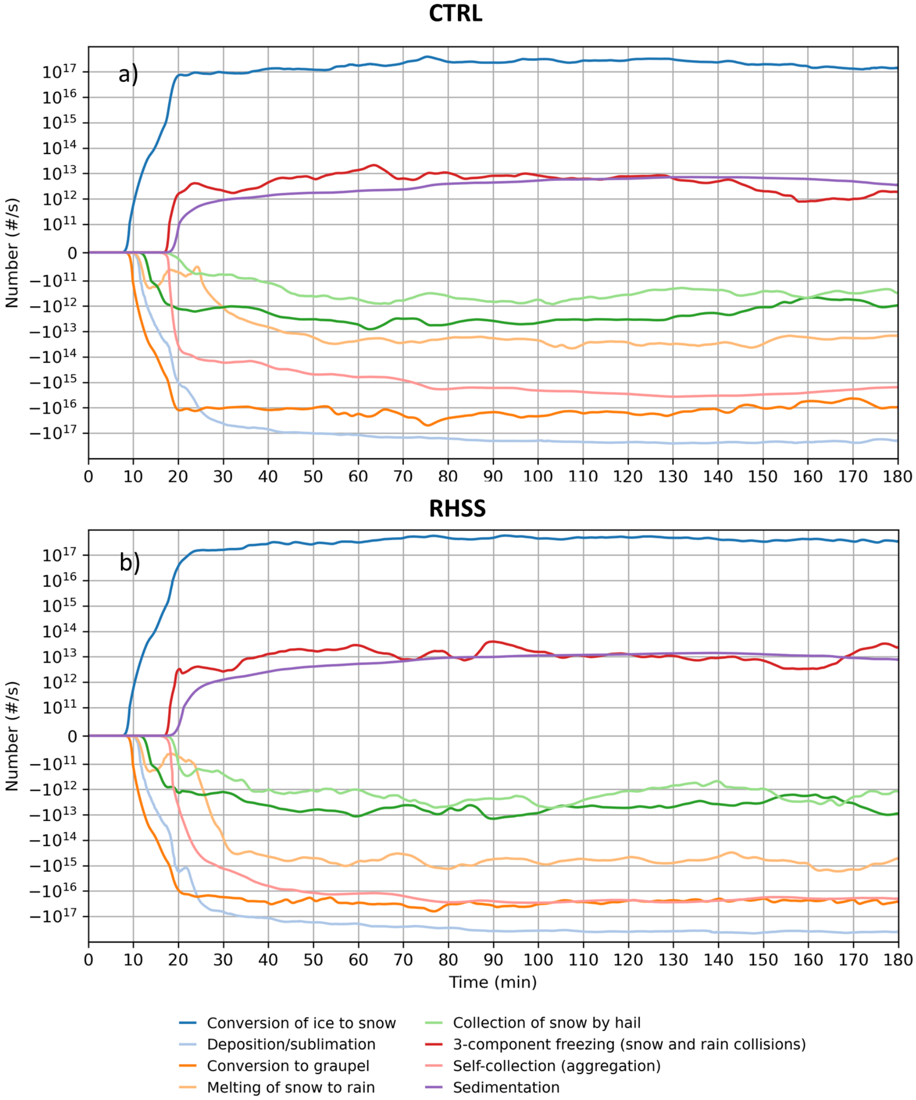

Figure 14. The time series of source/sink terms for the snow total number in the domain for CTRL **(a)** and RHSS **(b)** cases. Different microphysical processes are depicted with different colors indicated in the figure's legend at the bottom. The values of the quantities are averaged over 1 minute.

3.2.5 Graupel response

The conversion of snow to graupel (blue line in Fig. 15) is an important mechanism for graupel mass production resulting from cloud seeding (Fig. 6a). The same applies to the number of graupel particles (Fig. 16 and Fig. 6b). The largest responses were observed in the collection of ice crystals by graupel and the conversion of ice to graupel (purple and light red lines in Fig. 15, respectively). This suggests that a relatively small change in abundant cloud ice may have a relatively large effect on other hydrometeors, particularly their number.

Interaction among raindrops, cloud ice, snow, and graupel in the process of 3–component freezing also increased due to the presence of the reagent (red, light red, and purple lines in Fig. 16), as well as the conversion of ice to graupel (light green 410 line in Fig. 16). These processes have a greater influence on the number production of graupel compared to the mass. Furthermore, the two main sinks in graupel number, melting and sublimation (light orange and light blue in Fig. 13, respectively), have also increased due to seeding.

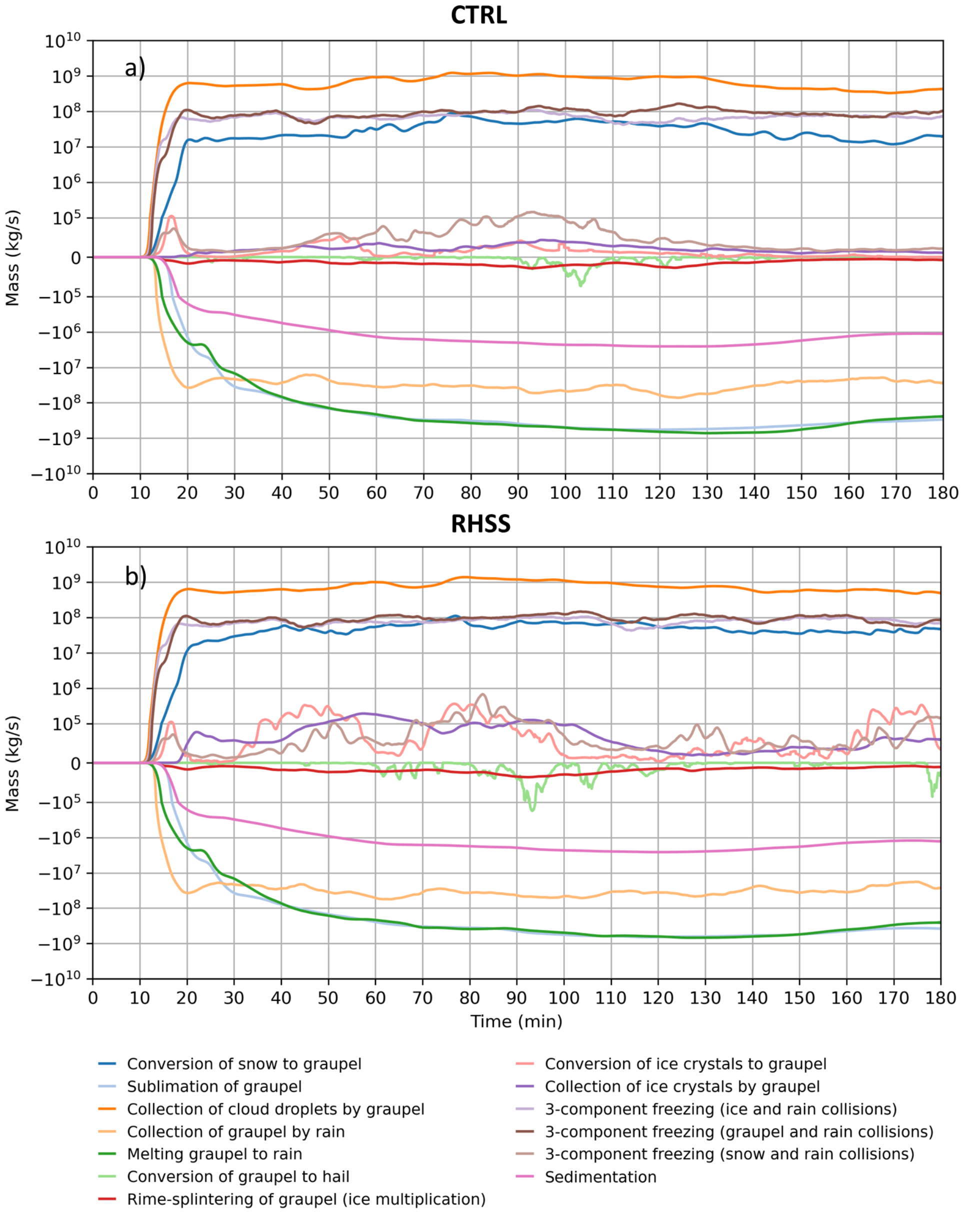

Figure 15. The time series of source/sink terms for the graupel total mass in the domain for CTRL **(a)** and RHSS **(b)** cases. Different 415 microphysical processes are depicted with different colors indicated in the figure's legend at the bottom. The values of the quantities are averaged over 1 minute.

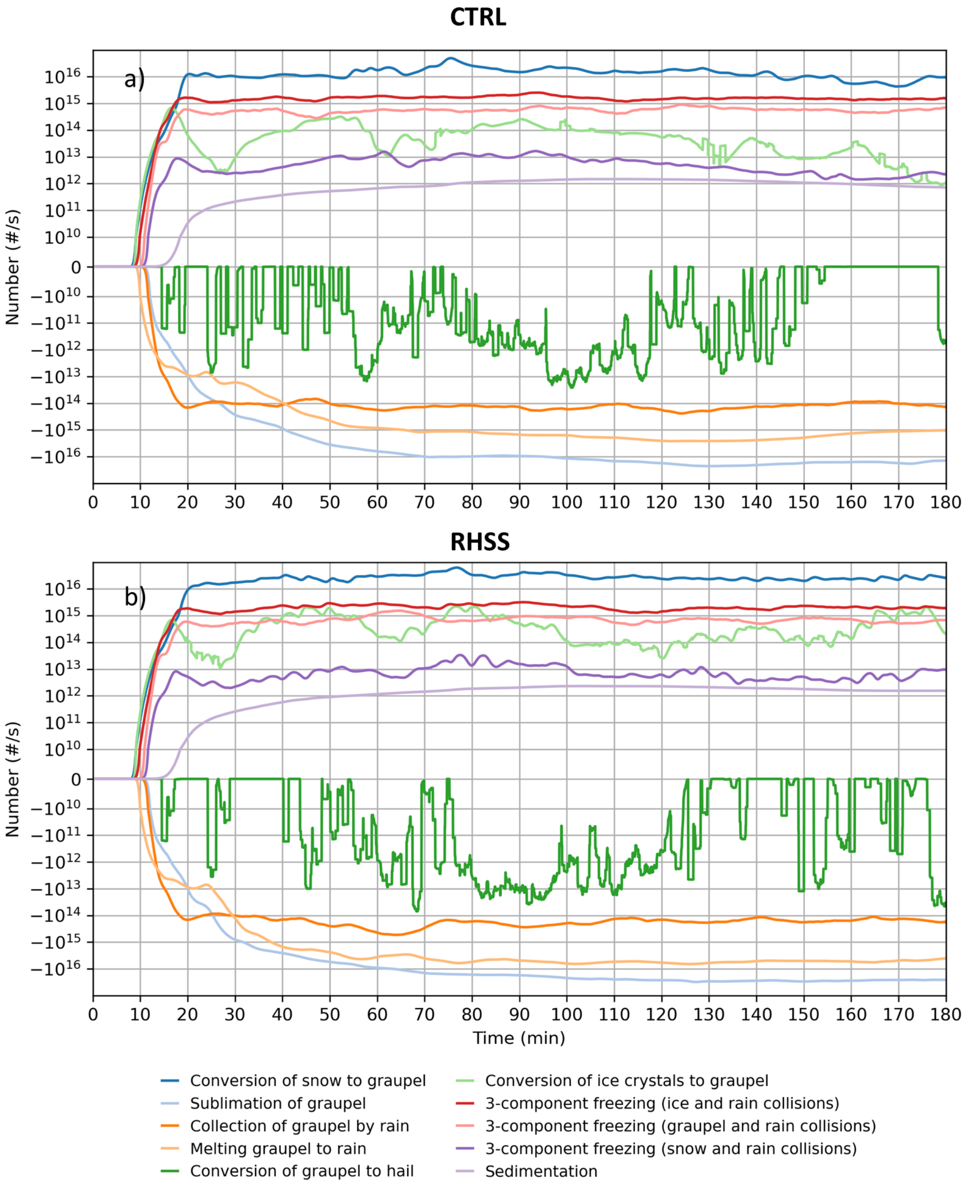

Figure 16. The time series of source/sink terms for the graupel total number in the domain for CTRL **(a)** and RHSS **(b)** cases. Different microphysical processes are depicted with different colors indicated in the figure's legend at the bottom. The values of the quantities are averaged over 1 minute.

3.2.6 Hail response

In this section, we finally examine in detail the effects of glaciogenic seeding on hail. Injected APs have produced a mixed effect on the total mass of hail (Fig. 6a) and a steady increase in the total number within the domain (Fig. 6b).

425 The changes in microphysics due to glaciogenic seeding for hail mass and number are shown in Figs. 17 and 18, respectively. The immersion freezing of raindrops has the most pronounced effect as a source of both hail mass (pink line in Fig. 17) and hail number (purple line in Fig. 18). Contact freezing of raindrops has a negligible influence on hail mass production (light brown line in Fig. 17) and, while significant, remains a smaller effect compared to immersion freezing on hail number (light red in Fig. 18).

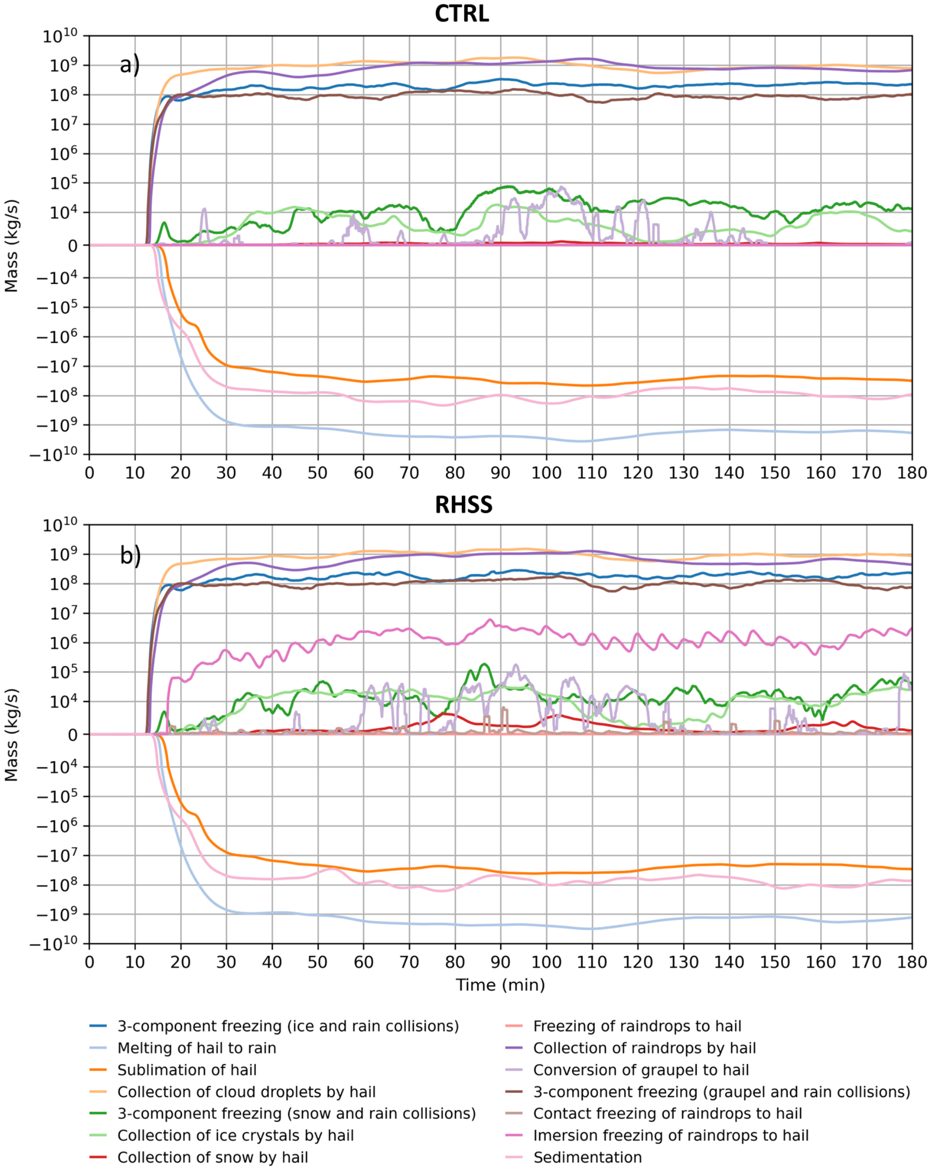

430

Figure 17. The time series of source/sink terms for the hail total mass in the domain for CTRL **(a)** and RHSS **(b)** cases. Different microphysical processes are depicted with different colors indicated in the figure's legend at the bottom. The values of the quantities are averaged over 1 minute.

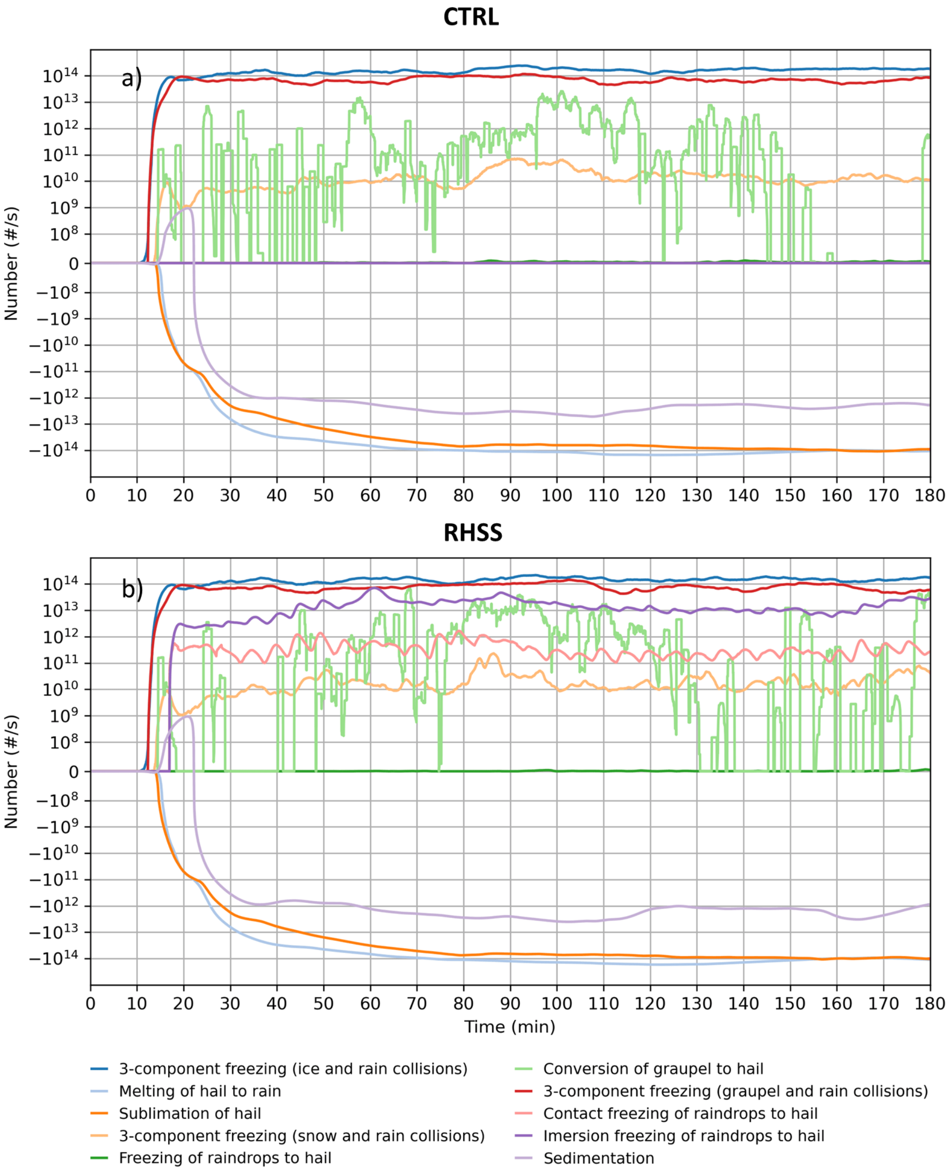

Figure 18. The time series of source/sink terms for the hail total number in the domain for CTRL **(a)** and RHSS **(b)** cases. Different microphysical processes are depicted with different colors indicated in the figure's legend at the bottom. The values of the quantities are averaged over 1 minute.

To assess the relative contributions of microphysical processes to hailstone mass and number, we examine the changes in these processes induced by seeding. Figure 19 shows the differences in the absolute values of source and sink term contributions between the RHSS and CTRL experiments.

If we disregard the processes with no clear response to seeding, that is, those with noise–like behaviour, we can draw several important conclusions about the effects of glaciogenic seeding:

- Immersion freezing of raindrops is the most important process as a source of hail, especially in terms of its number.
- Although contact freezing is negligible as a source of hail mass, it is very important as a source of hail number.
- Seeding caused a decrease in the melting of hail as a sink of hail mass and an increase in hail number, indicating a larger number of smaller hailstones.
- Sublimation as a sink term also played a significant role by decreasing the hailstone number after seeding.
- Due to the seeding, the collection of raindrops also undergoes a major decrease as a source term for the hail mass.
- Sedimentation as a sink term for hail number decreases significantly, indicating smaller hailstones.

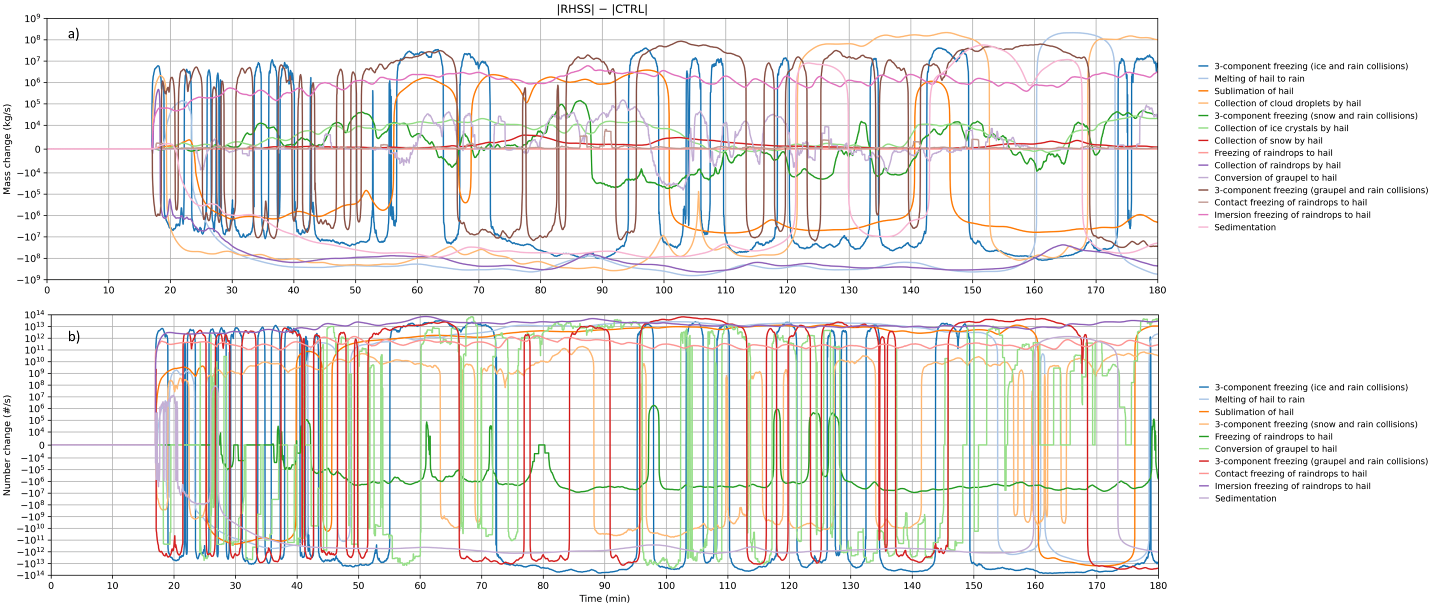

Figure 19. The time series of the difference in the absolute values of source/sink terms between RHSS and CTRL for the total hail mass **(a)** and number **(b)** in the domain. Different microphysical processes are depicted with different colors indicated in the figure's legend at the bottom. The values of the quantities are averaged over 1 minute.

From a perspective of hail suppression, the change in hail mean diameter ($D_h = (\frac{6Q_h\rho_a}{\pi\rho_h N_h})^{\frac{1}{3}}$) and its spatial distribution can be a valuable metric, where Q_h and N_h are the hail mixing ratio [kg kg^{-1}] and number concentration [m^{-3}], respectively, ρ_a air density [kg m^{-3}], and ρ_h=900 kg m^{-3} hail density.

The impact of glaciogenic seeding on the mean diameter of raindrops and hail, averaged over the entire domain for both RHSS and AB23 methodologies, is shown in Fig. 20 (left y–axis). Introducing AgI particles clearly affects the mean hail diameter, causing a decrease during the first 2 hours for both methods. After 130 minutes, this effect becomes less distinct. An even larger decrease in the mean raindrop diameter is evident, especially in the first 30 minutes after seeding initiation. This reduction in mean raindrop diameter can be attributed to increased melting of ice, snow, and graupel, which significantly raises the number of raindrops and thus decreases the mean diameter. Note that this represents the mean hail diameter calculated in a bulk microphysical model; consequently, these values are substantially smaller than 5 mm in diameter, which is a commonly used lower threshold for defining hail (Straka, 2009; Lohmann, 2016).

The total cumulative precipitation rainfall (blue lines) and hailfall (green lines) are also shown in Fig. 20 for all three experiments. Rainfall decreased for both the RHSS and AB23 methodologies as a result of the reduction in raindrop diameter. Total hailfall was also reduced by 26.4% and 17.7% in the RHSS and AB23 experiments, respectively.

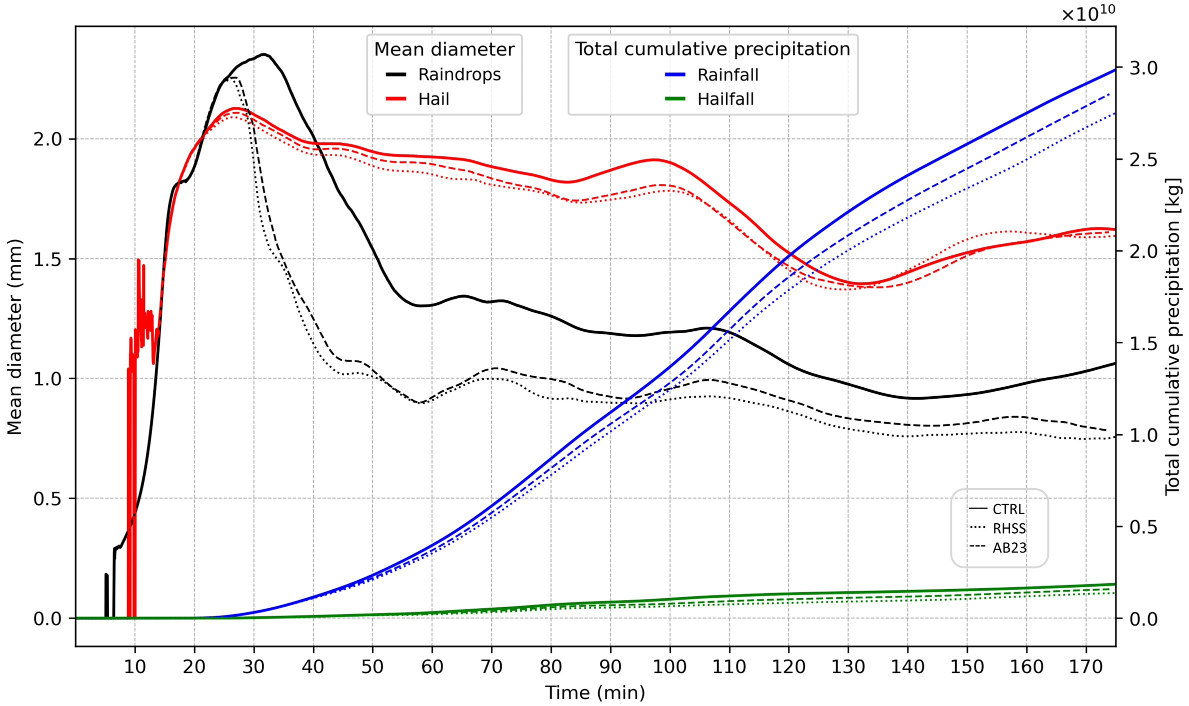

Figure 20. Time series of the mean diameter (mm) of raindrops (black) and hailstones (red), averaged over the entire model domain (left y–axis), for the CTRL (solid), RHSS (dotted), and AB23 (dashed) experiments. The total cumulative precipitation (kg) for rainfall (blue) and hailfall (green) is shown on the right y–axis.

3.3 Ground–Level Hail Characteristics

Regarding hail–induced damage, surface hail characteristics are most important. In this section, we examine the influence of glaciogenic cloud seeding on hail characteristics at the surface.

The most commonly used variable to assess the effectiveness of hail suppression is mean hail diameter (Papaevangelou et al., 2025; 2026). Figure 21 shows the change in mean hail diameter at the surface due to seeding for RHSS (a, c, and e) and AB23 (b, d, and f) at 60–minute intervals. The change is shown only in grid boxes with a liquid equivalent hailfall rate greater than 1 mm h^{-1}, to exclude irrelevant and artificial results caused by numerical reasons. The change in mean hail diameter across the entire surface domain is discussed in Appendix B. Isolines of hailfall intensity at 1 mm h^{-1}, 10 mm h^{-1}, and 100 mm h^{-1} are shown in green, orange, and black, respectively. The control experiment is plotted with a solid line, and RHSS and AB23 (SEED) with a dashed line. To provide more detail, we present the size distribution of hail for several grid boxes within characteristic regions (marked with an x and a capital letter). These grid boxes were selected to be as close as possible to the locations of the largest changes in mean diameter and the highest hailfall intensity.

At 60 minutes (Fig. 21 a, b), both methodologies show a significant decrease in the area with intense hailfall (> 100 mm h^{-1}) due to seeding. The left–moving cell, which was not seeded, experienced only a minor influence as a result of an early seeding. The maxima in the decrease of hail mean diameter largely overlap with the reduction in the area of intense hailfall. Examining the size distribution of hail at point A, there is a significant decrease in the number of large hailstones (> 2 cm), especially in the case of RHSS (by at least 8 orders of magnitude). Point B is characterised by an increase in large hailstones for both methodologies; however, the number of large hailstones in the seeding cases at point B remains smaller than in the CTRL case at point A. In both cases, seeding also caused the appearance of moderate hailfall (> 10 mm h^{-1}) in the south.

At 120 minutes (Fig. 21 c, d), there is no significant change in the area of intense hailfall in the RHSS case, while a decrease is observed in AB23. Additionally, almost the same size distribution is present at point A for all three experiments. In contrast, the most notable decrease in mean diameter around point C also coincides with a reduction in the number of large hailstones for both methodologies. The region of moderate hailfall further developed in the south due to the seeding. The seeding effect in this region is indicated by an increase in both the mean diameter of hailstones and the number of large hailstones. The size distribution of hail after seeding at point B is very similar to that of the CTRL case at point C.

At the end of the simulation (Fig. 21 e, f), the most complex pattern is observed. The greatest decrease in mean hail diameter coincides with the most intense hailfall in the CTRL case. Seeding caused the disappearance of large hailstones at point A, where most large hailstones were present in the CTRL. At point A, the number of hailstones with a diameter of about 1 cm in the seeded cases is equal to the number of hailstones with a diameter of about 4 cm in the CTRL case. Conversely, it triggered an increase in large hailstones in the regions around points B and C.

This complex behaviour of hail at the surface can be explained by seeding–induced shifting, stretching, and shrinking of the hail mixing ratio and number concentration fields, driven by a nonlinear microphysical response. Continuous injection of seeding material clearly alters the hydrometeor fields, their spatial distribution, and the locations of their maxima. Thermodynamic effects also influence the storm's updraft. Changes in the updraft magnitude at a given time, as well as changes in the location and position of the updraft axis caused by seeding, can alter the hail distribution at the ground. Phenomena characterised with such a small spatial scale, such as hailfall, may be very sensitive to these changes.

https://doi.org/10.5194/egusphere-2026-1411
Preprint. Discussion started: 8 April 2026

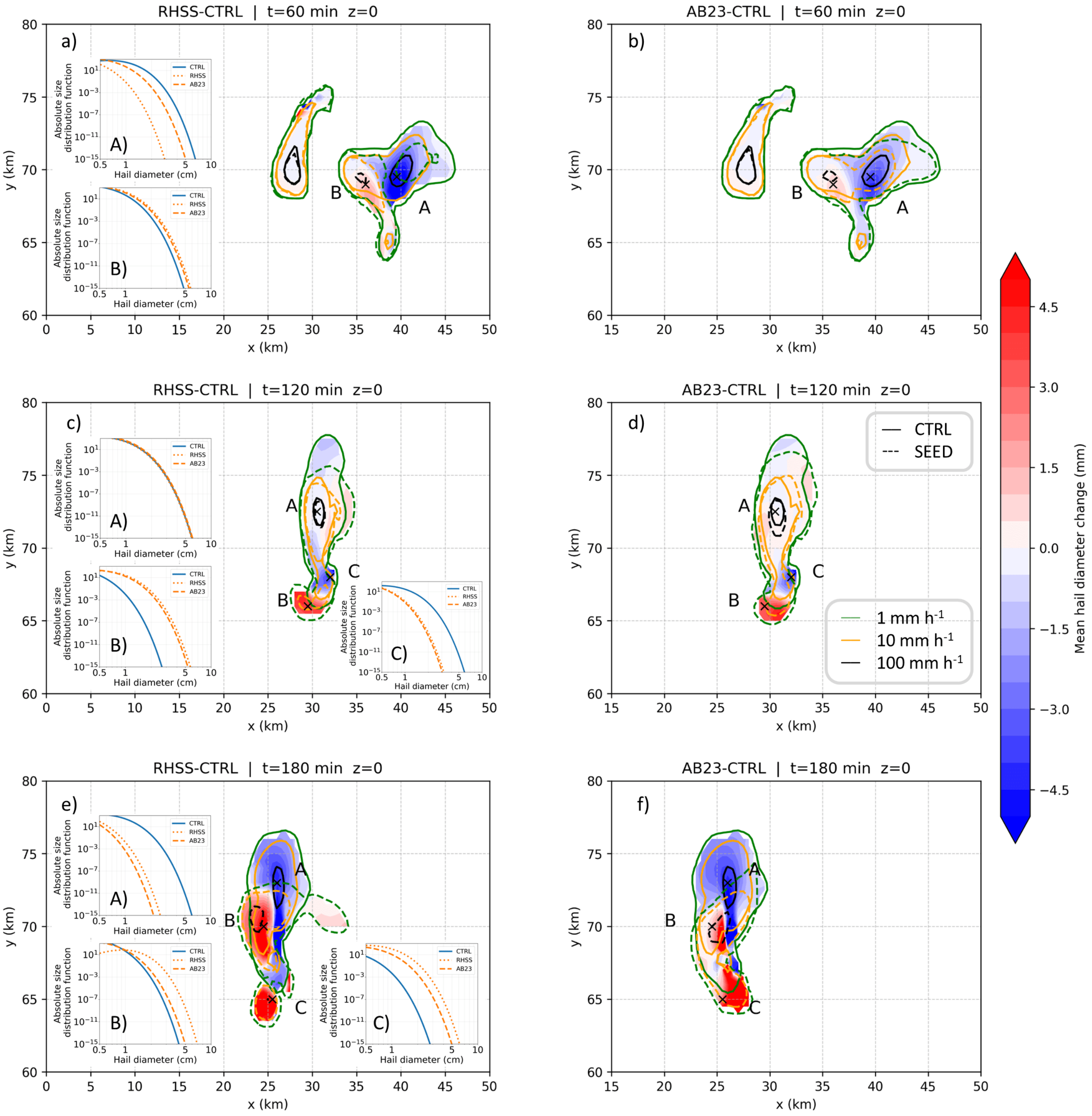

Figure 21. Changes in mean hail diameter at the surface (mm) at 1 h **(a, b)**, 2 h **(c, d)**, and 3 h **(e, f)**. The change is calculated by subtracting the CTRL mean hail diameter from that of each seeding methodology. RHSS is shown in the left panels **(a, c, e),** and AB23 in the right panels **(b, d, f)**. Only grid boxes with liquid equivalent hailfall intensity greater than 1 mm h⁻¹ are displayed. Isolines corresponding to hailfall intensities of 1 mm h⁻¹ (green), 10 mm h⁻¹ (orange), and 100 mm h⁻¹ (black) are shown as solid lines for the CTRL experiment and dashed lines for the seeded experiments (RHSS or AB23). Characteristic points of increase or decrease are marked by capital letters, for which the corresponding absolute hail size distributions [m^{-4}] are shown in the inset panels (blue solid line for CTRL, orange dotted line for RHSS, and orange dashed line for AB23).

https://doi.org/10.5194/egusphere-2026-1411
Preprint. Discussion started: 8 April 2026

Although examining the ground–level hail distribution is interesting, from the practical perspective of hail damage mitigation, it is more useful to consider integral quantities. For a given surface area covered by crops or infrastructure, in addition to hailstone size and concentration, the extent of hail damage also depends on the duration for which a given area is exposed to hailfall. As noted by Ursu et al. (2025), hail kinetic energy (KE) flux represents a suitable metric for damage assessment. It is considered that the threshold of 300 J m^{-2} of hail kinetic energy exposure identifies hail swaths with a high likelihood of crop damage. In Fig. 22, the hail kinetic energy flux in the CTRL case, integrated over the entire time period (3 h), is shown in red. The thresholds of 300 J m^{-2} and 100 J m^{-2} are indicated with orange and blue contours, respectively. The total KE flux exerted by this hailstorm (integrated over the entire surface) and the areas within these two thresholds are calculated and displayed in the title of Fig. 22. Comparing these variables may provide insight into the effect that glaciogenic seeding has on hail mitigation. The corresponding results for the seeding cases is shown in Fig. 23.

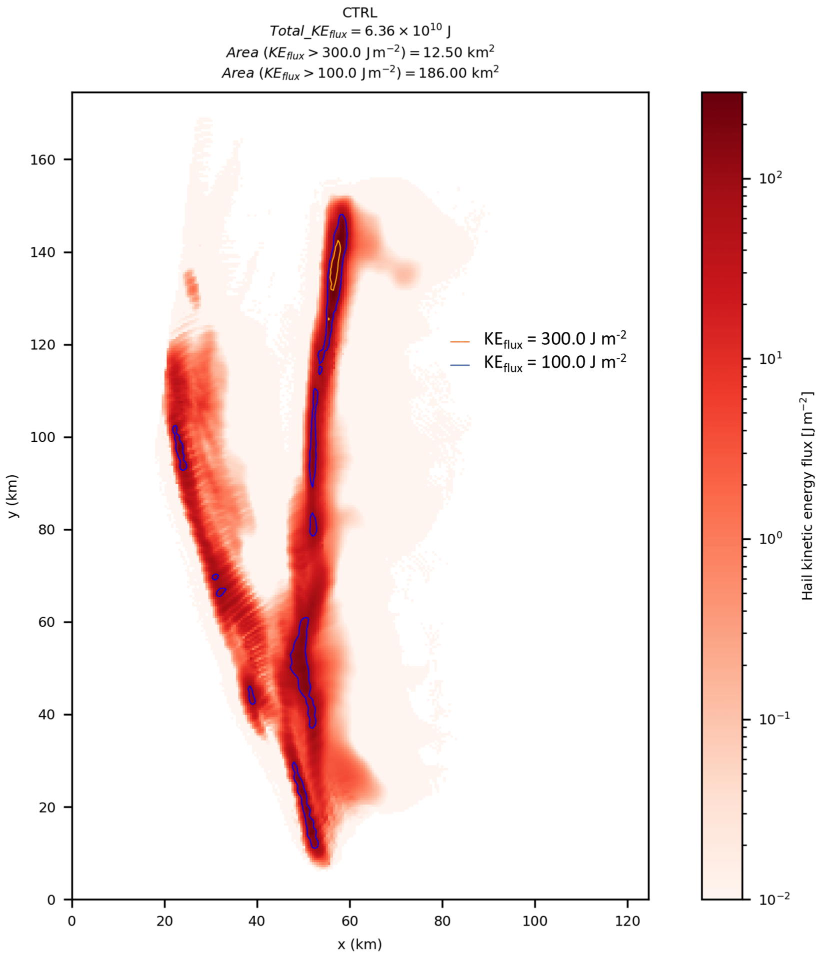
CTRL
$Total\_KE_{flux} = 6.36 \times 10^{10}$ J
$Area\ (KE_{flux} > 300.0\ \mathrm{J\,m^{-2}}) = 12.50\ \mathrm{km^2}$
$Area\ (KE_{flux} > 100.0\ \mathrm{J\,m^{-2}}) = 186.00\ \mathrm{km^2}$

Figure 22. Hail kinetic energy flux for the CTRL case integrated over the entire simulation period (red shading). Orange and blue contours denote values exceeding 300 J m^{-2} and 100 J m^{-2}, respectively. The domain–integrated total kinetic energy flux (3 h) and the areas exceeding these thresholds are reported in the figure title.

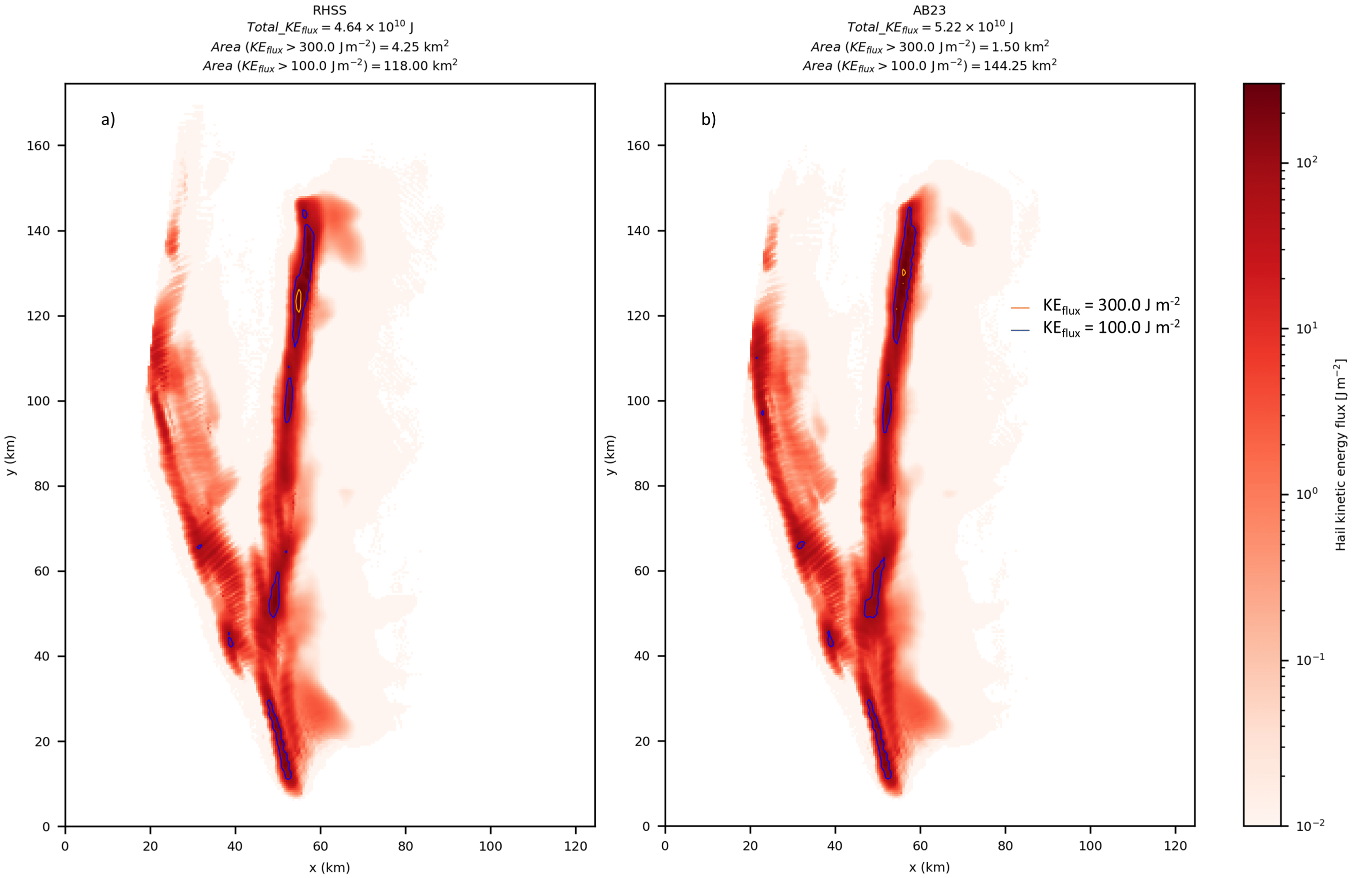

Figure 23. Hail kinetic energy flux for the RHSS **(a)** and AB23 **(b)** case integrated over the entire simulation period (red shading). Orange and blue contours denote values exceeding 300 J m^{-2} and 100 J m^{-2}, respectively. The domain–integrated total kinetic energy flux (3 h) and the areas exceeding these thresholds are reported in the figure title.

In the CTRL experiment, the hail exerted the total of 6.36·10^{10} J of KE during 3 hours over the entire surface area. The surface area most impacted by hailfall (KE$_{flux}$ > 300 J m^{-2}) is 12.5 km^{2,} and that of a less potential for crop damage (KE$_{flux}$ > 100 J m^{-2}) is 186 km^2. As can be seen from Table 4, all three quantities have decreased as a result of seeding.

Table 4: Kinetic energy flux for different experiments. The changes of seeding cases compared to CTLR are given in brackets.

	CTRL	RHSS	AB23
Area (KE$_{flux}$ > 300 J m^{-2})	12.5 km^2	4.25 km^2 (−66%)	1.5 km^2 (−88%)
Area (KE$_{flux}$ > 100 J m^{-2})	186 km^2	118 km^2 (−36.6%)	114.25 km^2 (−38.6%)
Total KE$_{flux}$	6.36·10^{10} J	4.64·10^{10} J (−27%)	5.22·10^{10} J (−17.9%)

The total KE_{flux} decreased by 27% for the RHSS and 17.9% for the AB23. The area of moderate hail kinetic energy ($KE_{flux} >$ 100 J m^{-2}) decreased approximately by the same amount for both methodologies, 36.6% and 38.6% for the RHSS and the AB23, respectively. Furthermore, the area with hailfall that has the most potential to cause damage ($KE_{flux} >$ 300 J m^{-2}) decreased significantly. This decrease is 66% in the case of RHSS and 88% for AB23. The data presented here are consistent with the beneficial competition hypothesis for hail suppression, in that glaciogenic seeding has little effect on overall hailfall but reduces its most extreme impacts.

4. Discussion

This research is focused on a case study of a well–known supercell storm. To account for the wide range of hailstorm types and the various climatological factors influencing their formation, a broader scientific approach is necessary. Supercell clouds are intense, long–lived, quasi–stationary weather systems with significant potential to produce hailfall and consequent damage to crops and infrastructure. The response to seeding in this particular type of convective systems may differ from other types. This idealized approach requires a sensitivity study to assess the effects of deviations in operational practice as well as to evaluate potential improvements to the methodology.

Conversely, the approach presented by Papaevangelou et al. (2026) has proven to be a robust method for addressing the variability of these processes. By employing ensemble modeling on several hailstorms and averaging microphysical and dynamical characteristics of the storm, detailed research on sensitivity and the range of these characteristics can be conducted.

To date, methods for evaluating the effect of cloud seeding for hail suppression have been mainly statistical. Current knowledge of cloud physics, numerical models, and computational capabilities enables in–depth investigation of the physical processes involved in cloud seeding through explicit numerical experiments. Although such numerical results are valuable for understanding cloud response to seeding, field campaigns are necessary for comparison.

It is also important to highlight the limitations of this approach. Evaluating the effectiveness of operational cloud seeding using numerical methods can be very challenging. Many variables typically not accounted for in numerical models, such as the spatial and temporal variability of environmental cloud condensation nuclei (CCN) (Kovačević, 2023), may introduce significant uncertainty and affect the effectiveness of hail mitigation techniques. Furthermore, the parameterization of AgI nucleation exhibits considerable variability (Marcolli et al., 2016; Miller et al., 2025). The activation of aerosol particles (APs) depends on the chosen parameterization, size distribution, and chemical composition, while the scavenging rate of APs also plays a crucial role in cloud seeding. Verifying these parameterizations in real clouds, particularly convective clouds, remains extremely challenging, introducing additional non–negligible uncertainty (Wang et al., 2010; Zhang et al., 2013).

5. Conclusion

In this study, we used a three–dimensional cloud–resolving numerical model, based on three–moment microphysics, with an added two–moment aerosol parameterization, to simulate the microphysical response and evaluate the impact of glaciogenic cloud seeding on hailfall characteristics. Highly explicit numerical simulations were conducted. The model setup was designed to follow two seeding methodology procedures for identifying the type of convective process, determining a seeding zone, and automatically injecting the prescribed mass of glaciogenic material. The aerosols in the model followed a gamma distribution and had the characteristics of silver iodide. All known scavenging mechanisms were included. This allowed a detailed investigation of the chain of events related to cloud seeding, from the AP injection followed by their scavenging and redistribution within each hydrometeor category, then their nucleation by one of four nucleation modes, and finally their effects on microphysics. Two different operational methodologies were employed (the RHSS and the AB23), and their effects were compared.

This methodology demonstrated promising results in detecting the microphysical response induced by ice–nucleating particles and, consequently, their influence on broader hailfall characteristics relevant to hail damage mitigation.

Here, we present the most important effects of seeding in this case:

- An insignificant decrease in the total hail mass is observed during the first 2 h of integration, followed by a slight increase thereafter. In contrast, the total number of hailstones steadily increases during the first 2 h in the RHSS case, with negligible change afterward, while for AB23 it continues to increase throughout the entire integration period.
- Immersion freezing of raindrops is the dominant source of hail change, particularly governing hail number, while contact freezing contributes negligibly to hail mass but remains an important source of hail number. Seeding modifies the hail population primarily by reducing sedimentation, reducing the hail mass loss by melting and increasing its number loss. Weakening of raindrop collection as a mass source is observed, while sublimation clearly increased the hail number loss due to seeding. Collectively, these changes indicate a shift toward a larger number of smaller hailstones under seeded conditions.
- The total cumulative hailfall (in kg) has decreased as a result of seeding by 26.4% for RHSS and 17.7% for AB23.
- The hail size distribution on the surface showed a significant complexity. An overall decrease in the number of large hailstones is present, although an appearance of large hailstones was also observed in the regions with no hail in the CTRL case. The continuous seeding with glaciogenic material caused a shift and deformation of hydrometeor and updraft fields, therefore, a point–for–point comparison may not provide an expected or easy–to–interpret result.
- The total hail kinetic energy exerted on the surface decreased by 27% and 17.9% for the RHSS and the AB23, respectively.
- The area of a moderate potential with hail–induced crop damage ($KE_{flux} > 100$ J m^{-2}) decreased by 36.6% and 38.6% for the RHSS and the AB23, respectively.

- This decrease in high potential damage area ($KE_{flux} > 300$ J m^{-2}) decreased by 66% and 88% for the RHSS and the AB23, respectively.

This study presents a model–based approach to evaluate the effectiveness of hail suppression and examines two operational methodologies. The results indicate a reduction in hail–induced crop damage, as indicated by hail kinetic energy analysis, for both methodologies, consistent with findings reported by Dessens et al. (2016) and Garstang et al. (2005). However, the findings of this case study may not be applicable to the full range of convective cloud types and environmental conditions associated with hailstorm formation. Therefore, more generalized studies are required, along with radar, in situ, and surface measurements to verify the model results.

Acknowledgements

This research was funded by the Science Fund of the Republic of Serbia, No. 7389, Project "Extreme weather events in Serbia—analysis, modelling and impacts"—EXTREMES.

Code and data availability

The model output data are archived and deposited at Harvard Dataverse and are available to reviewers during the peer-review process or upon request. The dataset will be assigned a permanent DOI and will be publicly available upon acceptance of the manuscript. The ARPS model (version 5.4.3) is publicly accessible at https://arps.caps.ou.edu/arpsdown.html, along with the sounding data used in this study.

Competing interests

The authors declare that they have no competing interests.

Author contributions

Darko Savić: Conceptualization, Data curation, Formal analysis, Investigation, Methodology, Software, Visualization, Writing (original draft preparation).
Vladan Vučković: Investigation, Methodology, Software, Supervision
Dragana Vujović: Investigation, Methodology

Appendix A

635 This appendix presents a microphysical diagnostic obtained using the AB23 methodology. Figures A1–A13 correspond to Fig. 7–19 from the Results section. Due to the large number of figures, the results for the AB23 methodology are presented separately here. Comparison of these results shows a similar overall influence of seeding in both cases.

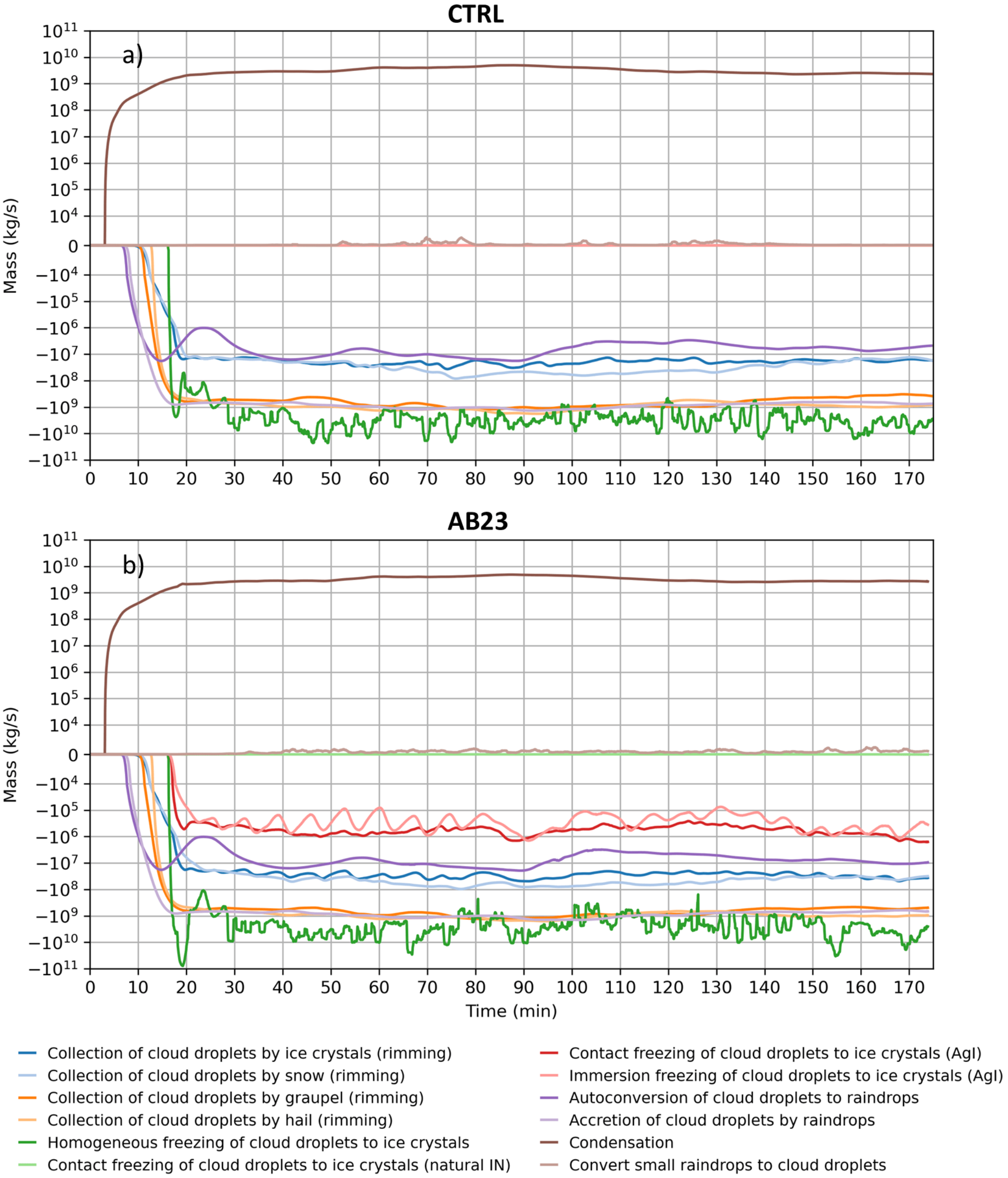

Figure A1. The time series of source/sink terms for the cloud droplet total mass in the domain for CTRL **(a)** and AB23 **(b)** cases. Different 640 microphysical processes are depicted with different colors indicated in the figure's legend at the bottom. The values of the quantities are averaged over 1 minute.

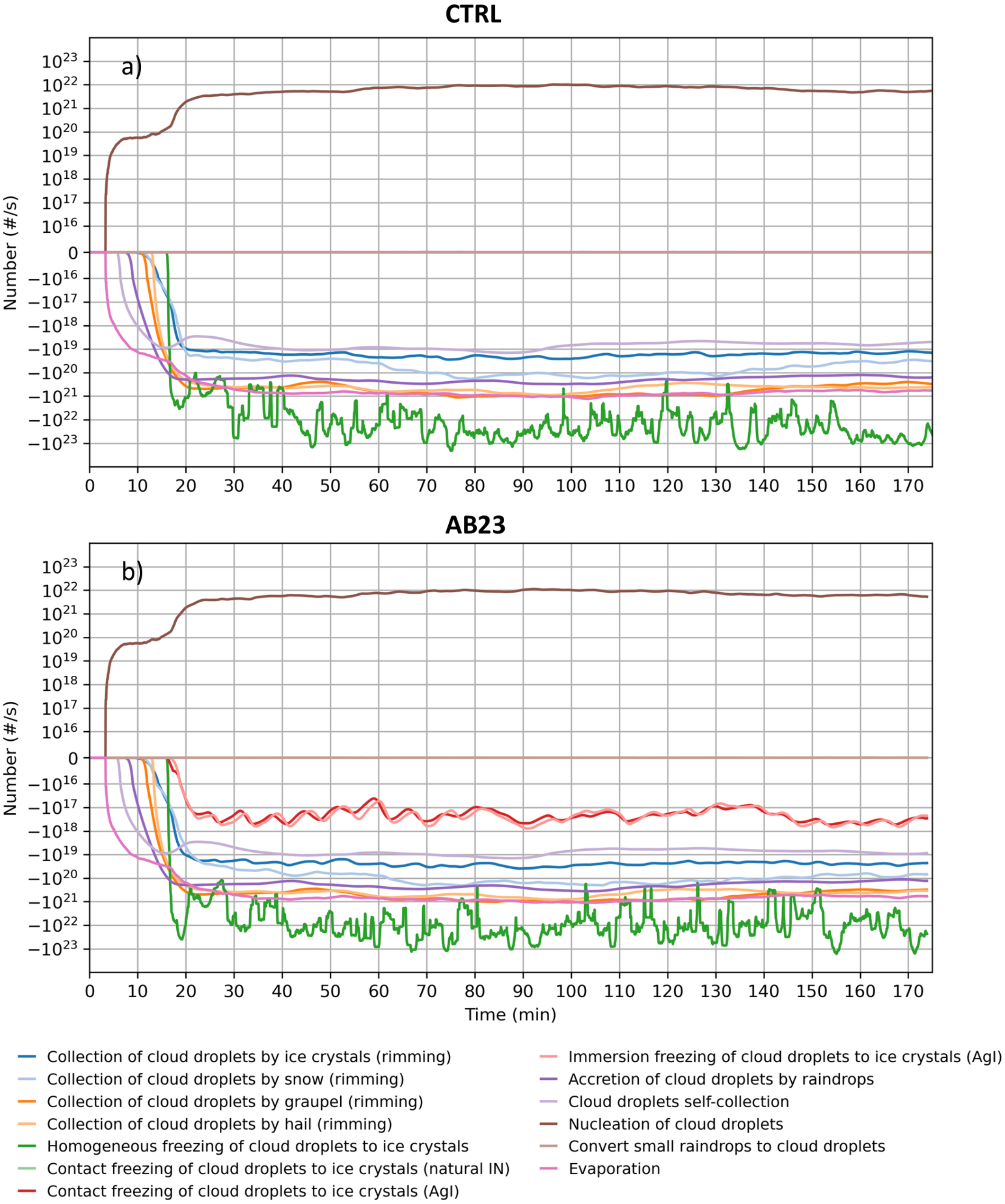

Figure A2. The time series of source/sink terms for the cloud droplet total number in the domain for CTRL **(a)** and AB23 **(b)** cases. Different microphysical processes are depicted with different colors indicated in the figure's legend at the bottom. The values of the quantities are averaged over 1 minute.

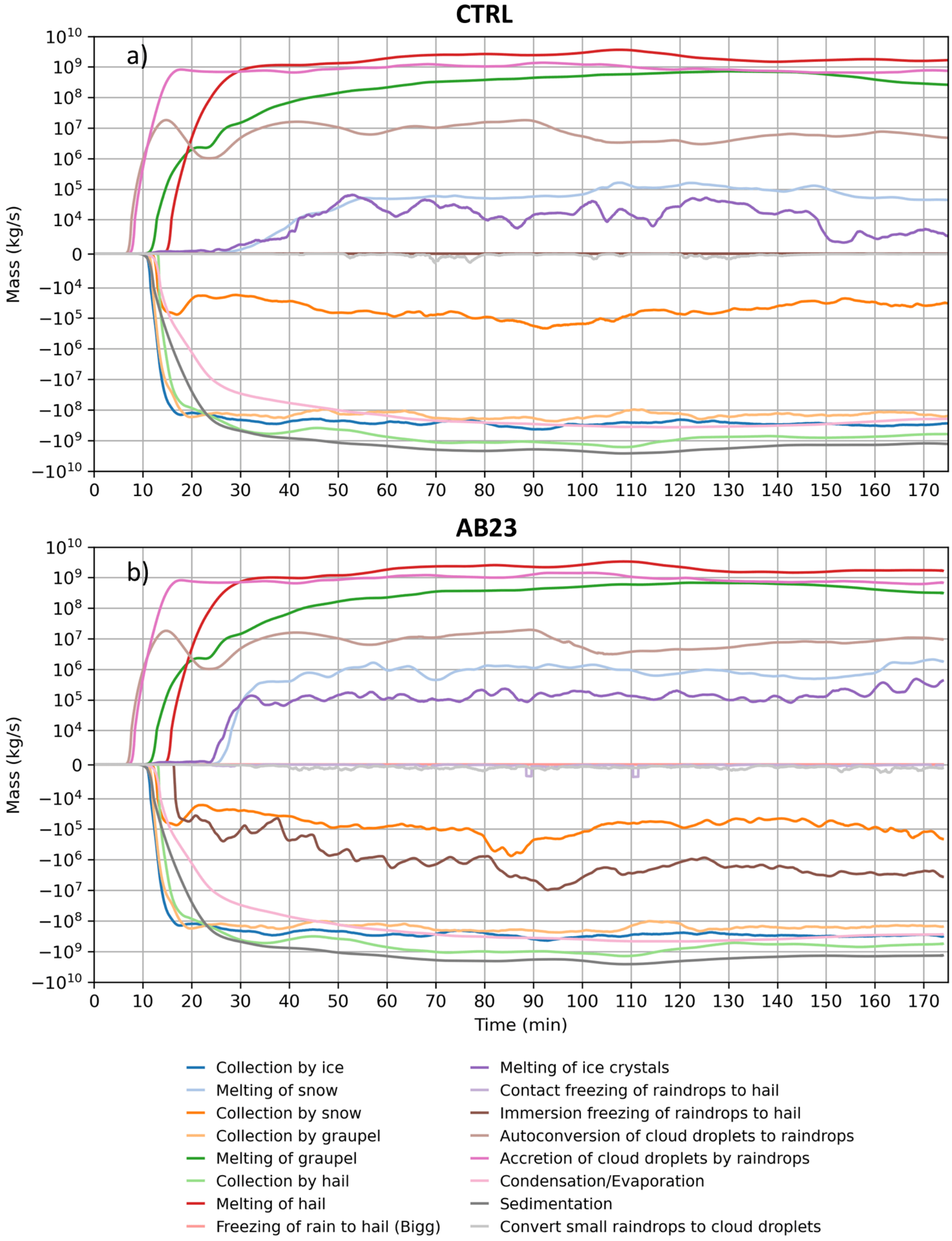

Figure A3. The time series of source/sink terms for the raindrops total mass in the domain for CTRL **(a)** and AB23 **(b)** cases. Different microphysical processes are depicted with different colors indicated in the figure's legend at the bottom. The values of the quantities are averaged over 1 minute.

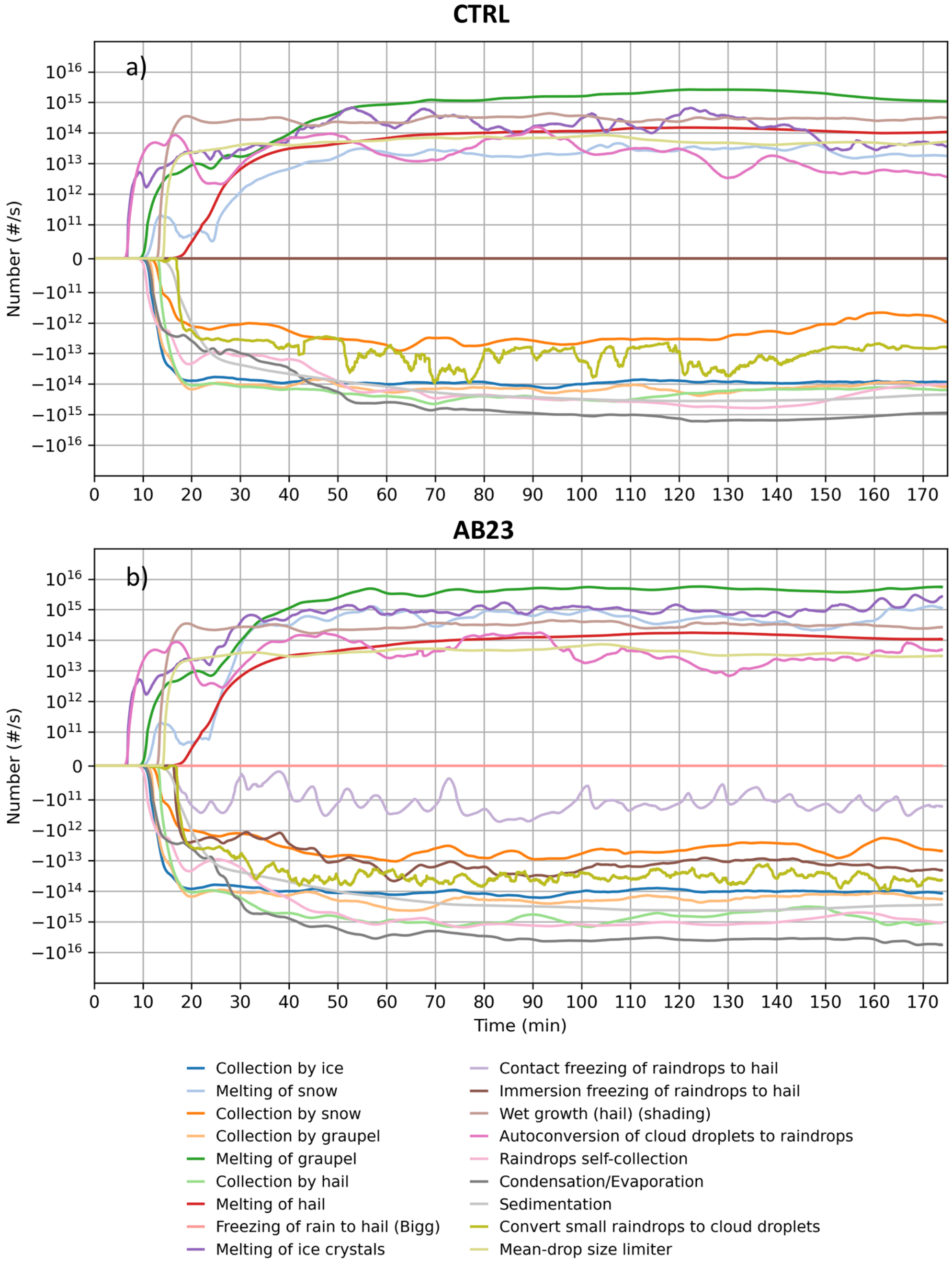

Figure A4. The time series of source/sink terms for the raindrops total number in the domain for CTRL **(a)** and AB23 **(b)** cases. Different microphysical processes are depicted with different colors indicated in the figure's legend at the bottom. The values of the quantities are averaged over 1 minute.

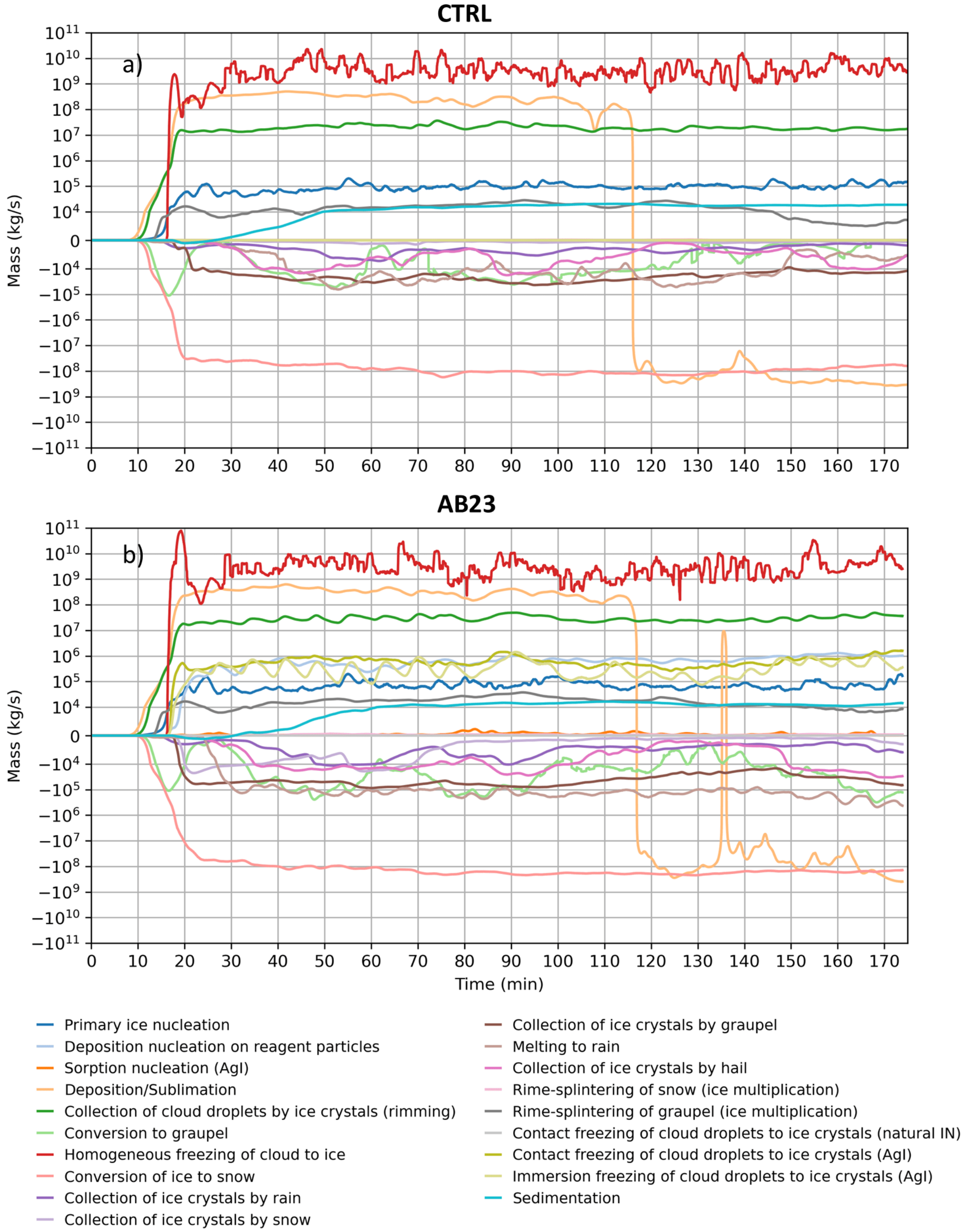

Figure A5. The time series of source/sink terms for the cloud ice total mass in the domain for CTRL **(a)** and AB23 **(b)** cases. Different microphysical processes are depicted with different colors indicated in the figure's legend at the bottom. The values of the quantities are averaged over 1 minute.

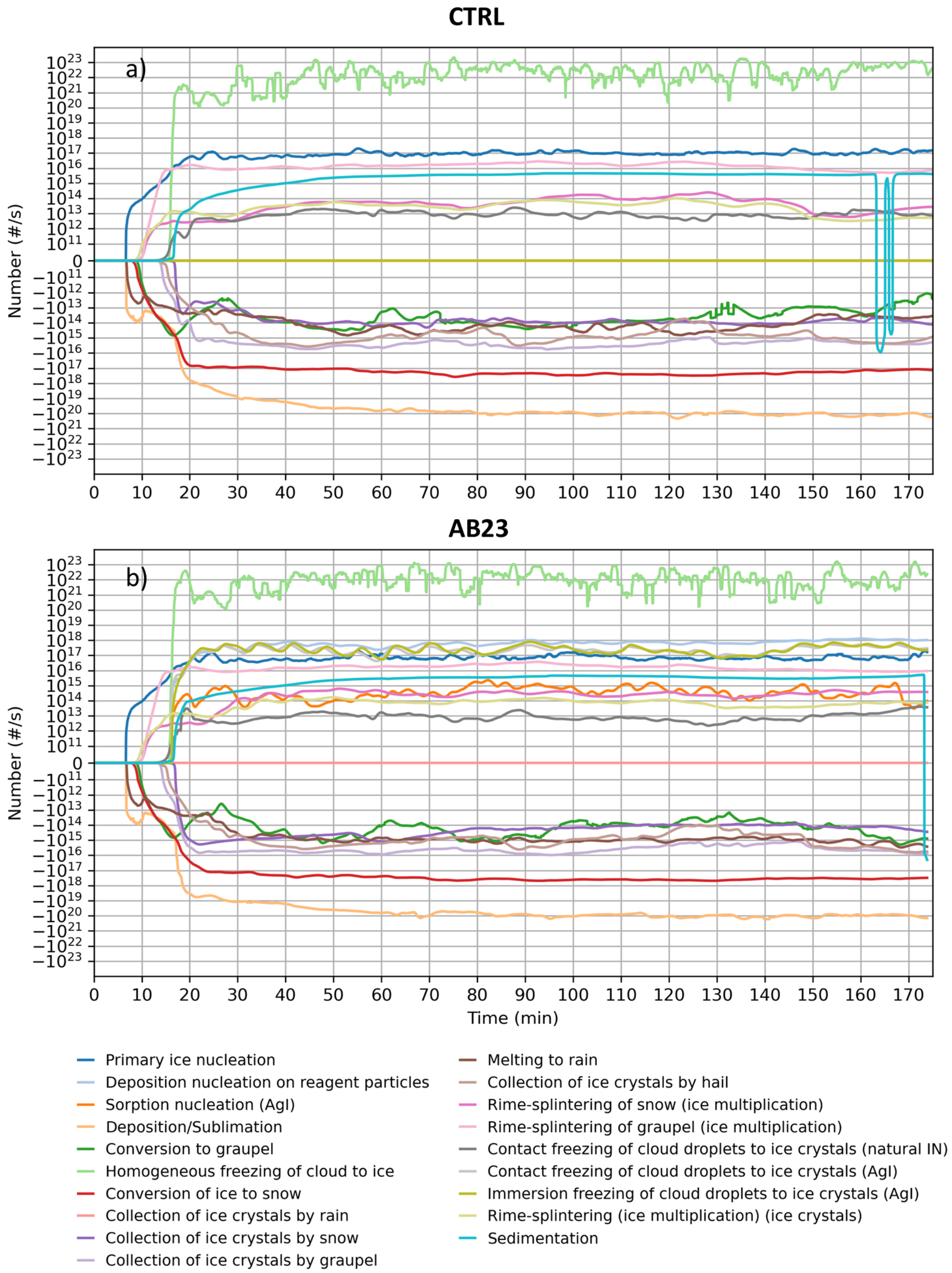

Figure A6. The time series of source/sink terms for the cloud ice total number in the domain for CTRL **(a)** and AB23 **(b)** cases. Different microphysical processes are depicted with different colors indicated in the figure's legend at the bottom. The values of the quantities are averaged over 1 minute.

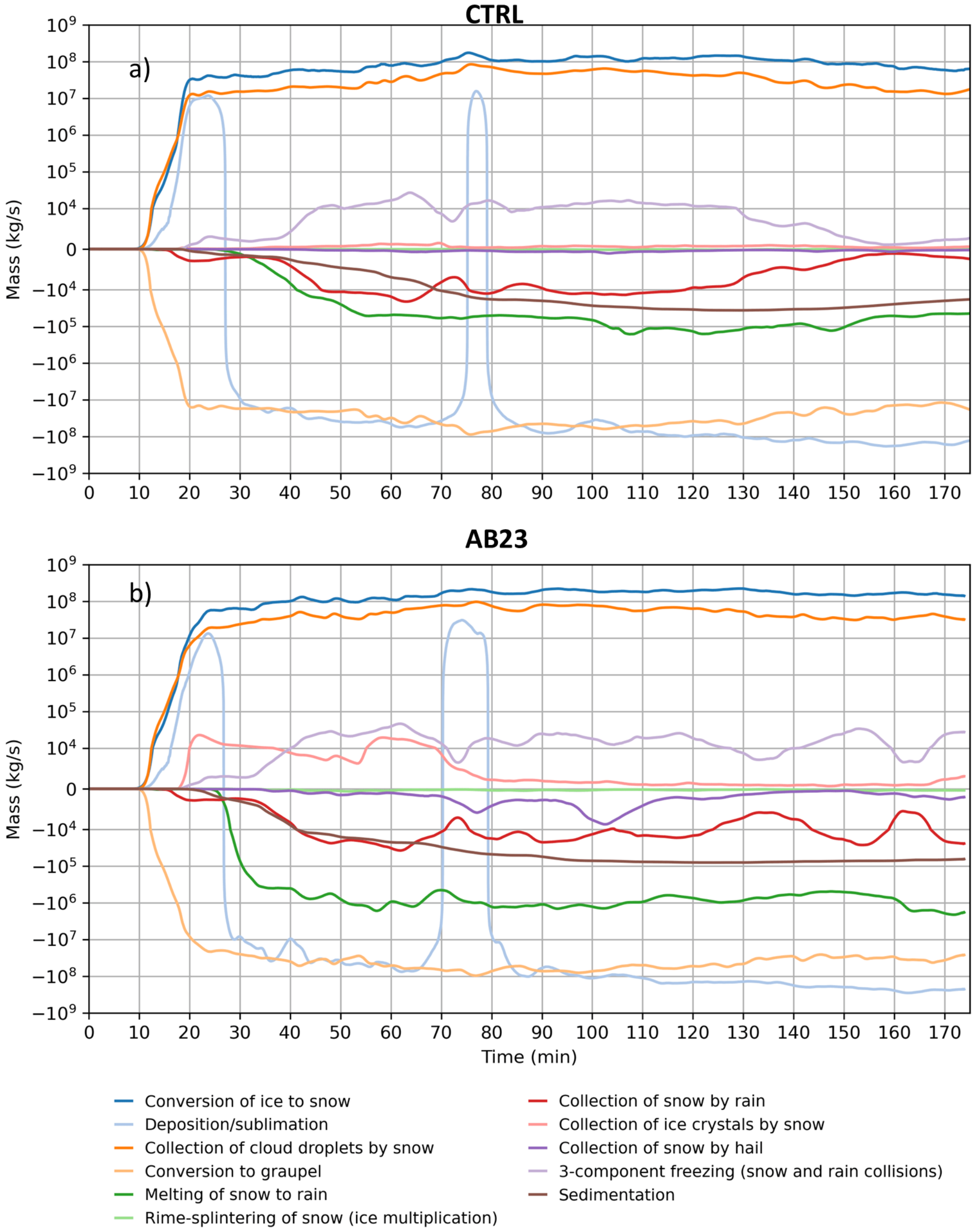

665 **Figure A7**. The time series of source/sink terms for the snow total mass in the domain for CTRL **(a)** and AB23 **(b)** cases. Different microphysical processes are depicted with different colors indicated in the figure's legend at the bottom. The values of the quantities are averaged over 1 minute.

https://doi.org/10.5194/egusphere-2026-1411
Preprint. Discussion started: 8 April 2026

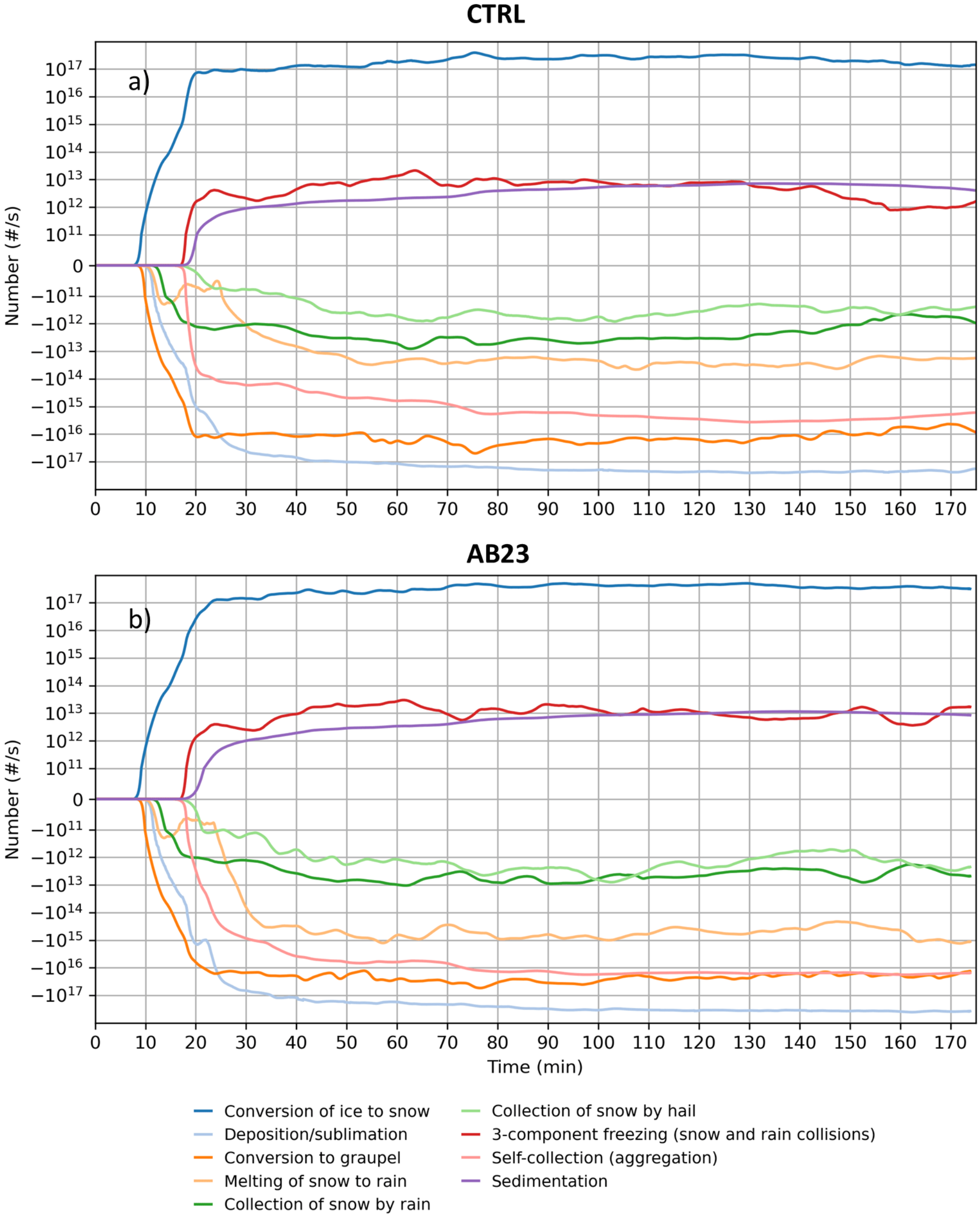

670 **Figure A8**. The time series of source/sink terms for the snow total number in the domain for CTRL **(a)** and AB23 **(b)** cases. Different microphysical processes are depicted with different colors indicated in the figure's legend at the bottom. The values of the quantities are averaged over 1 minute.

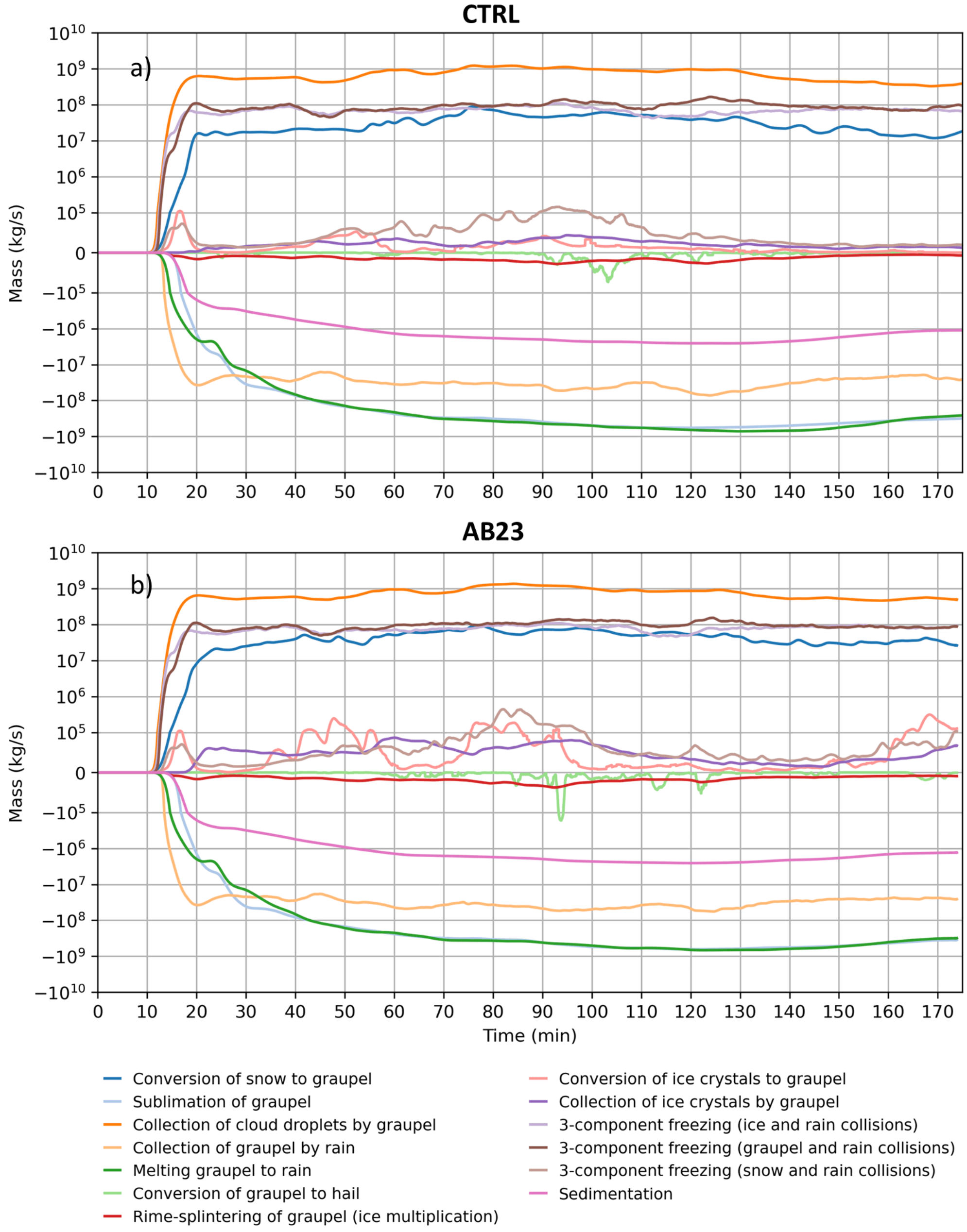

675 **Figure A9**. The time series of source/sink terms for the graupel total mass in the domain for CTRL **(a)** and AB23 **(b)** cases. Different microphysical processes are depicted with different colors indicated in the figure's legend at the bottom. The values of the quantities are averaged over 1 minute.

https://doi.org/10.5194/egusphere-2026-1411
Preprint. Discussion started: 8 April 2026

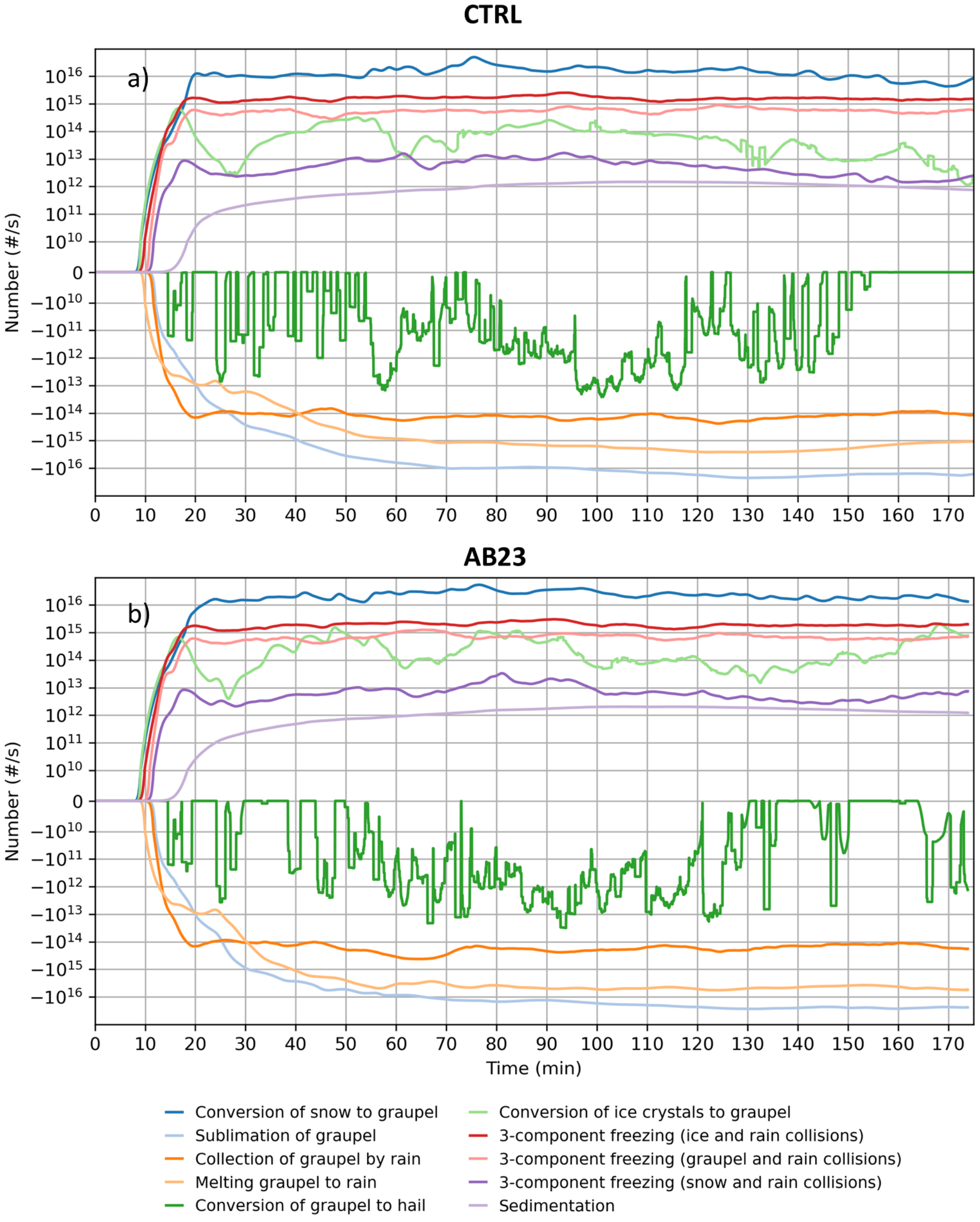

Figure A10. The time series of source/sink terms for the graupel total number in the domain for CTRL **(a)** and AB23 **(b)** cases. Different microphysical processes are depicted with different colors indicated in the figure's legend at the bottom. The values of the quantities are averaged over 1 minute.

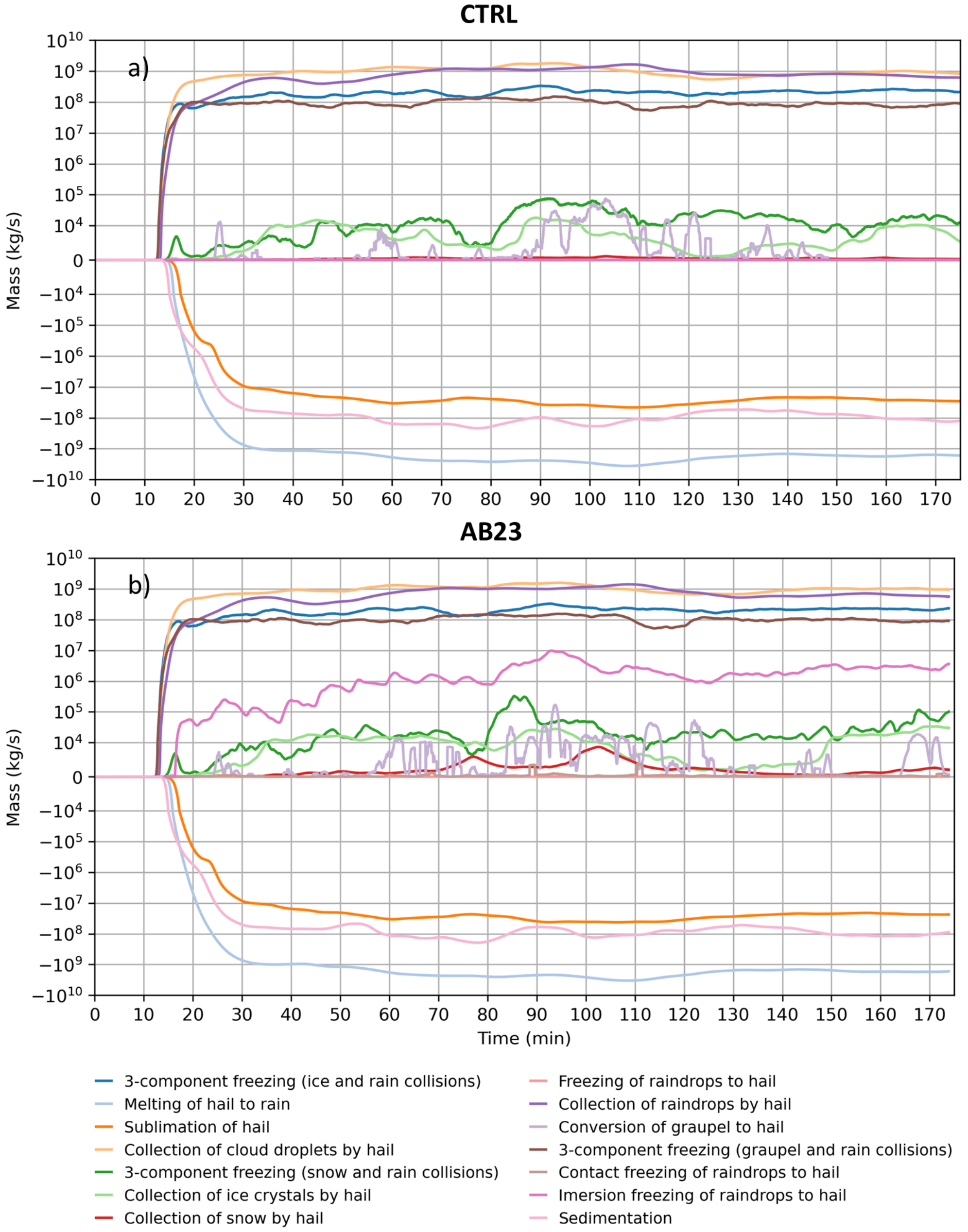

685 **Figure A11**. The time series of source/sink terms for the hail total mass in the domain for CTRL **(a)** and AB23 **(b)** cases. Different microphysical processes are depicted with different colors indicated in the figure's legend at the bottom. The values of the quantities are averaged over 1 minute.

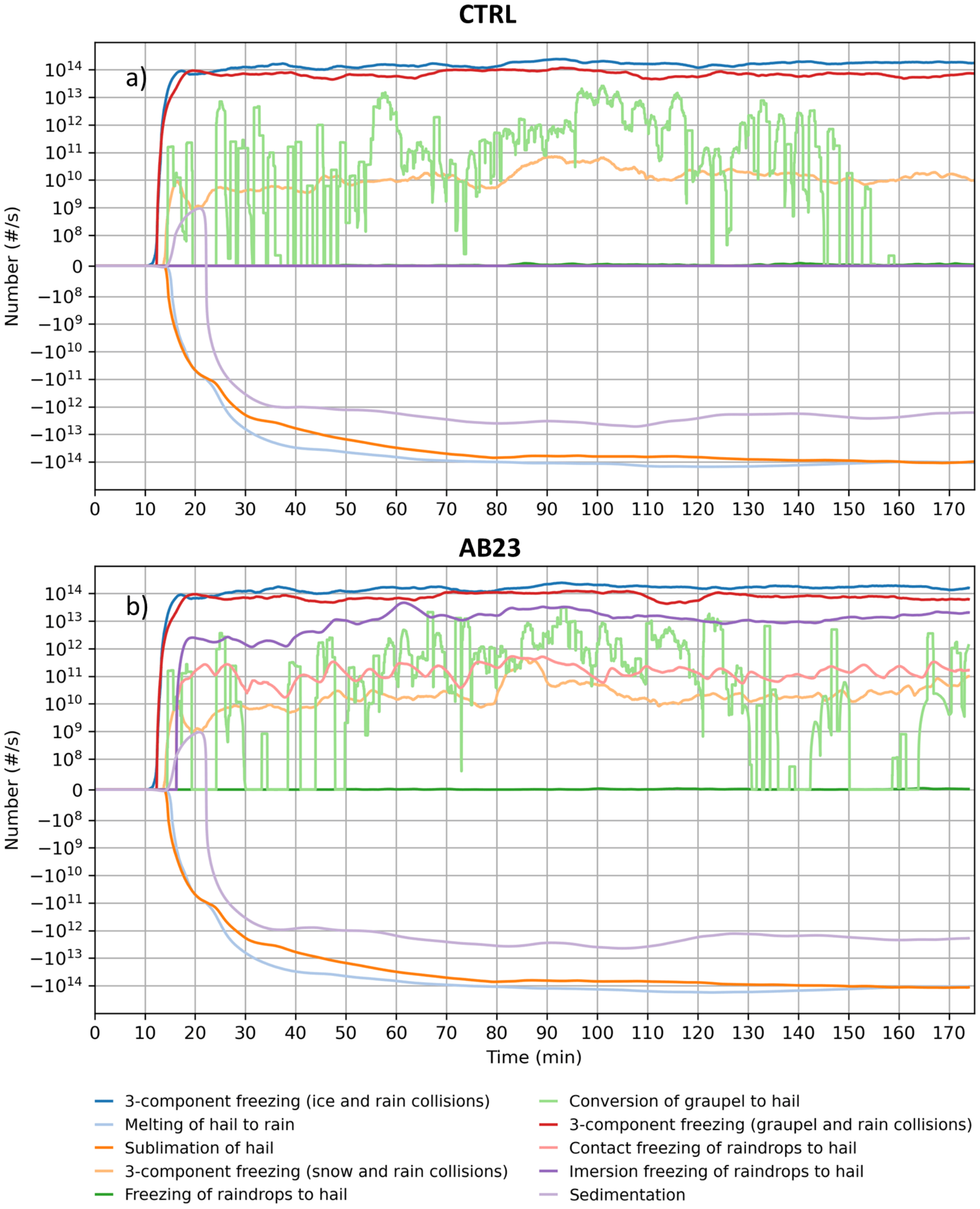

Figure A12. The time series of source/sink terms for the hail total number in the domain for CTRL **(a)** and AB23 **(b)** cases. Different microphysical processes are depicted with different colors indicated in the figure's legend at the bottom. The values of the quantities are averaged over 1 minute.

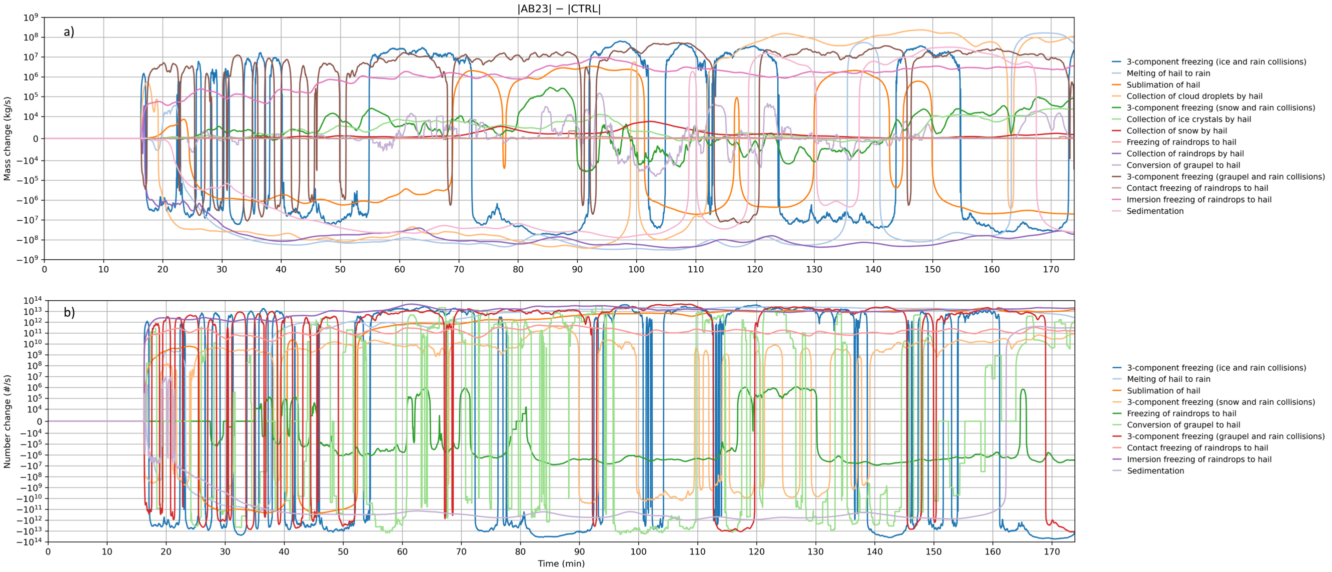

Figure A13. The time series of the difference in the absolute values of source/sink terms between AB23 and CTRL for the total hail mass in the domain **(a)** and number **(b)**. Different microphysical processes are depicted with different colors indicated in the figure's legend at the right. The values of the quantities are averaged over 1 minute.

Appendix B

The change in the mean diameter of hail at the surface, caused by seeding, for both methodologies and at 60–minute intervals, is shown in Fig. 21. Blue colors indicate regions where the mean diameter decreased as a result of seeding, while red indicates regions where it increased. Both RHSS (Fig. B1 a, c, and e) and AB23 (Fig. B1 b, d, and f) show similar patterns. Examining the hail size distribution in more detail makes this pattern clearer. We selected locations within the characteristic regions of mean hail diameter increase or decrease (marked with an x and a capital letter) to analyse changes in hail size distribution (see the inset panels in Fig. B1, labeled with the corresponding capital letter for each grid box).

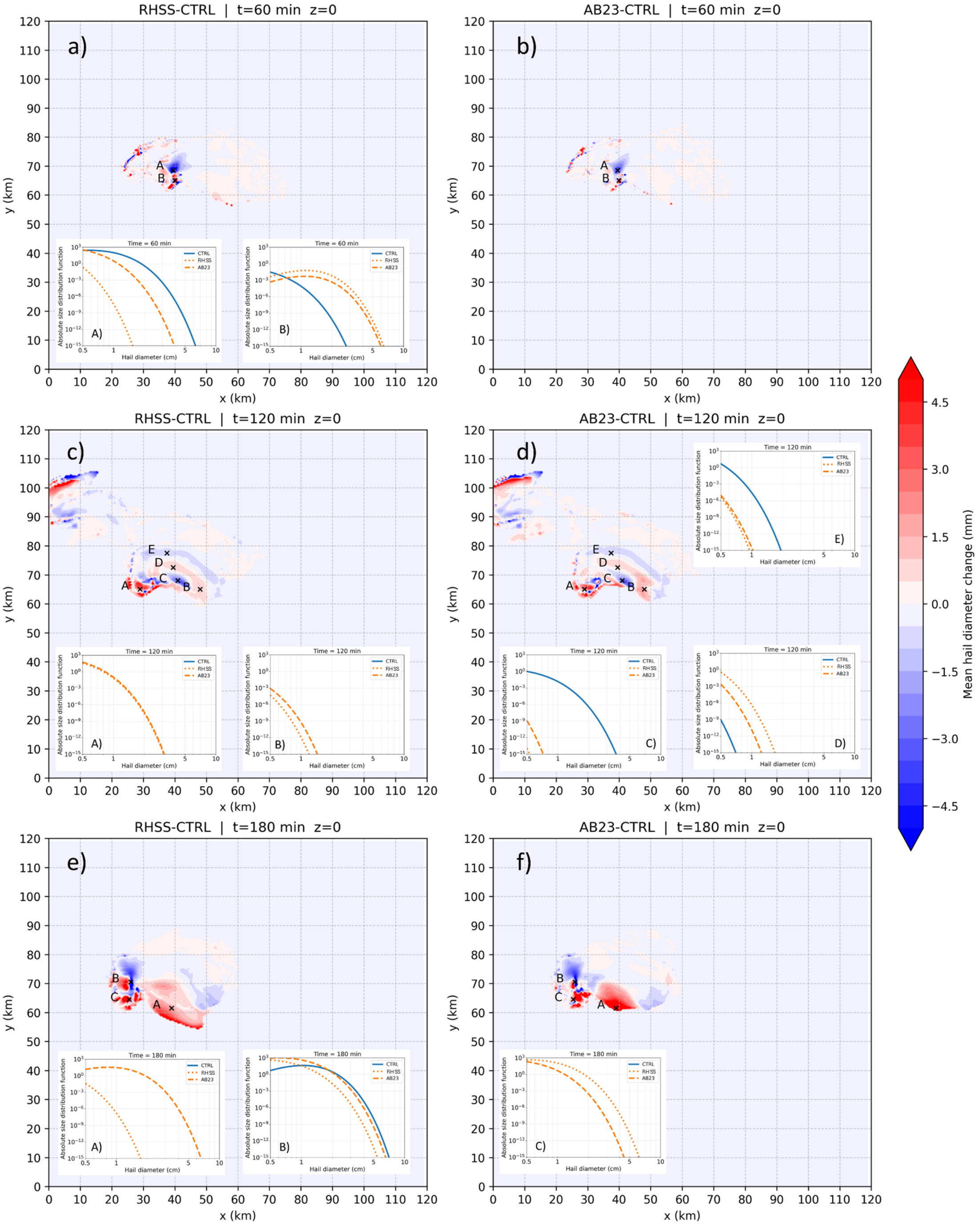

Figure B1. Changes in mean hail diameter at the surface (mm) at 1 h **(a, b)**, 2 h **(c, d)**, and 3 h **(e, f)**. The change is calculated by subtracting the CTRL mean hail diameter from that of each seeding methodology. RHSS is shown in the left panels **(a, c, e),** and AB23 in the right panels **(b, d, f)**. Characteristic points of increase or decrease are marked by capital letters, for which the corresponding absolute hail size distributions [m^{-4}] are shown in the inset panels (blue solid line for CTRL, orange dotted line for RHSS, and orange dashed line for AB23).

At 60 minutes (Fig. B1 a and b), two regions with relatively large changes in mean hail diameter are evident. A decrease in mean diameter occurs at point A. Comparison with the CTRL experiment (blue solid line in subplot A) shows that seeding with the RHSS method (orange dotted line) and AB23 (orange dashed line) shifts the hail size distribution towards smaller diameters, consistent with effective hail suppression in this case. Large hailstones (>2 cm) are much less frequent as a result of seeding, especially with RHSS. The region of mean hail diameter increase (subplot B) shows a significant rise in the number of large hailstones, thus increasing the mean diameter as well. However, comparison of points A and B shows that, in both seeding cases, the number of hailstones of a given size at point B is reduced relative to CTRL at point A; slightly for large hailstones and by 4–5 orders of magnitude for small hailstones.

At 120 minutes (Fig. B1 c and d), a more complex pattern emerges. The areas of mean diameter decrease, around points C and E, show a significant reduction in the number of hailstones, especially the large ones. This is particularly notable at point C, which contained a relatively large number of hailstones in the CTRL experiment, whereas seeding completely eradicated hail at this location. Conversely, an increase in mean diameter at points B and D is related to the appearance of hail in areas otherwise without hail. These areas have no significant hailfall after seeding and can be disregarded for the purpose of this work. A considerable amount of hail appeared in the area around point A. In the CTRL experiment, there was no hail at this point. The hail size distribution at point A in the RHSS and AB23 cases is similar to that of the CTRL case at point C, although point C contains more large hailstones (by an order of magnitude).

At the end of integration (180 min), three distinct areas of mean diameter change are again observed (Fig. B1 e and f). A significant decrease is seen in and around point B. The expected impact of seeding is evident here, with a decrease in the number of large hailstones and an increase in the number of small ones. Furthermore, seeding triggered the formation of a significant amount of hail at points A and C, where no hail was present in the CTRL experiment. In both points, large hailstones are much less frequent compared to CTRL at point B.

References

Abshaev, A. M., Abshaev, M. T., Malkarova, A. M., and Barekova, M. V.: Guidelines for the Organization and Conduct of Antihail Works, Printing House, Nalchik, Russia, 508 pp., 2014.

Abshaev, M. T., Abshaev, A. M., and Malkarova, A. M.: Results of 65-Years Project of Hail Suppression in Russian Federation, in: Physics of the Atmosphere, Climatology and Environmental Monitoring, edited by: Zakinyan, R. and Zakinyan, A., Springer Proceedings in Earth and Environmental Sciences, Springer, Cham, https://doi.org/10.1007/978-3-031-19012-4_1, 2023.

American Society of Civil Engineers: Guidelines for Operational Hail Suppression Programs, American Society of Civil Engineers, 2015.

Brandes, E. A.: Finestructure of the Del City–Edmond tornadic mesocirculation, Mon. Weather Rev., 109, 635–647, 1981.

Brooks, H. E., Lee, J. W., and Craven, J. P.: The spatial distribution of severe thunderstorm and tornado environments from global reanalysis data, Atmos. Res., 67–68, 73–94, https://doi.org/10.1016/S0169-8095(03)00045-0, 2003.

Ćurić, M., Janc, D., and Vučković, V.: Seeding agent dispersion within convective cloud as simulated by a 3-D numerical model, Meteorol. Atmos. Phys., 92, 205–216, 10.1007/s00703-005-0159-2, 2006.

Ćurić, M., Janc, D., and Vučković, V.: Cloud seeding impact on precipitation as revealed by cloud-resolving mesoscale model, Meteorol. Atmos. Phys., 95, 179–193, 10.1007/s00703-006-0202-y, 2007.

Ćurić, M., Janc, D., and Vučković, V.: Precipitation change from a cumulonimbus cloud downwind of a seeded target area, J. Geophys. Res., 113, D11215, https://doi.org/10.1029/2007JD009483, 2008.

Ćurić, M., Janc, D., Vučković, V., and Kovačević, N.: An inadvertent transport of the seeding material as a result of cloud modification, Meteorol. Atmos. Phys., 105, 157–165, https://doi.org/10.1007/s00703-009-0040-9, 2009.

DeMott, P. J.: A characterization of mixed silver iodide–silver chloride ice nuclei, M.S. thesis, Department of Atmospheric Science, Colorado State University, 124 pp., 1982.

DeMott, P. J.: Quantitative descriptions of ice formation mechanisms of silver iodide-type aerosols, Atmos. Res., 38, 63–99, https://doi.org/10.1016/0169-8095(94)00088-U, 1995.

Dessens, J., Sánchez, J. L., Berthet, C., Hermida, L., and Merino, A.: Hail prevention by ground-based silver iodide generators: Results of historical and modern field projects, Atmos. Res., 170, 98–111, https://doi.org/10.1016/j.atmosres.2015.11.008, 2016.

Garstang, M., Bruintjes, R., Serafin, R., Orville, H., Boe, B., Cotton, W., and Warburton, J.: Weather modification: Finding common ground, Bull. Am. Meteorol. Soc., 86, 647–655, https://doi.org/10.1175/BAMS-86-5-647, 2005.

Gillett, K. J.: SounderPy: An atmospheric sounding visualization and analysis tool for Python, J. Open Source Softw., 10, 8087, https://doi.org/10.21105/joss.08087, 2025.

Khain, A., Ovtchinnikov, M., Pinsky, M., Pokrovsky, A., and Krugliak, H.: Notes on the state-of-the-art numerical modeling of cloud microphysics, Atmos. Res., 55, 159–224, https://doi.org/10.1016/S0169-8095(00)00064-8, 2000.

Klemp, J. B., Wilhelmson, R. B., and Ray, P. S.: Observed and numerically simulated structure of a mature supercell thunderstorm, J. Atmos. Sci., 38, 1558–1580, 1981.

Klemp, J. B. and Rotunno, R.: A study of the tornadic region within a supercell thunderstorm, J. Atmos. Sci., 40, 359–377, 1983.

Kovačević, N.: Hail suppression effectiveness for varying solubility of natural aerosols in water, Meteorol. Atmos. Phys., 131, 585–599, https://doi.org/10.1007/s00703-018-0587-4,2019.

Kovačević, N.: Hail suppression effectiveness for different cloud condensation nucleus (CCN) populations in continental and maritime environments, Aerosol Sci. Technol., 57, 645–664, https://doi.org/10.1080/02786826.2023.2208182, 2023.

Loftus, A. M.: A triple-moment bulk hail microphysics scheme to investigate the sensitivities of hail to aerosols, Ph.D. thesis, Colorado State University, 2012.

Lohmann, U., Lüönd, F., and Mahrt, F.: An Introduction to Clouds: From the Microscale to Climate, Cambridge University Press, 391 pp., 2016.

Lompar, M., Ćurić, M., Romanic, D., Zou, L., and Liang, H.: Precipitation enhancement by cloud seeding using the shell structured TiO2/NaCl aerosol as revealed by new model for cloud seeding experiments, Atmos. Res., 212, 202–212, https://doi.org/10.1016/j.atmosres.2018.05.021, 2018.

Marcolli, C., Nagare, B., Welti, A., and Lohmann, U.: Ice nucleation efficiency of AgI: review and new insights, Atmos. Chem. Phys., 16, 8915–8937, 10.5194/acp-16-8915-2016,2016.

Mesinger, F. and Mesinger, N.: Has hail suppression in eastern Yugoslavia led to a reduction in the frequency of hail?, J. Appl. Meteor., 31, 104–111, https://doi.org/10.1175/1520-0450(1992)031<0104:HHSIEY>2.0.CO;2, 1992.

Meyers, M. P., DeMott, P. J., and Cotton, W. R.: A comparison of seeded and nonseeded orographic cloud simulations with an explicit cloud model, J. Appl. Meteorol., 34, 834–846, https://www.jstor.org/stable/26187222, 1995.

Milbrandt, J. A. and Yau, M. K.: A multimoment bulk microphysics parameterization. Part I: Analysis of the role of the spectral shape parameter, J. Atmos. Sci., 62, 3051–3064, https://doi.org/10.1175/JAS3534.1, 2005a.

Milbrandt, J. A. and Yau, M. K.: A multimoment bulk microphysics parameterization. Part II: A proposed three-moment closure and scheme description, J. Atmos. Sci., 62, 3065–3081, https://doi.org/10.1175/JAS3535., 2005b.

Milbrandt, J. A. and Yau, M. K.: A multimoment bulk microphysics parameterization. Part III: Control simulation of a hailstorm, J. Atmos. Sci., 63, 3114–3136, https://doi.org/10.1175/JAS3816.1, 2006a.

Milbrandt, J. A. and Yau, M. K.: A multimoment bulk microphysics parameterization. Part IV: Sensitivity experiments, J. Atmos. Sci., 63, 3137–3159, https://doi.org/10.1175/JAS3817.1, 2006b.

Miller, A. J., Fuchs, C., Ramelli, F., Zhang, H., Omanovic, N., Spirig, R., and Henneberger, J.: Quantified ice-nucleating ability of AgI-containing seeding particles in natural clouds, Atmos. Chem. Phys., 25, 5387–5407, 2025.

Moeng, C.-H. and Wyngaard, J. C.: Evaluation of turbulent transport and dissipation closures in second-order modeling, J. Atmos. Sci., 46, 2311–2330, 1989.

Morrison, H., van Lier-Walqui, M., Fridlind, A. M., Grabowski, W. W., Harrington, J. Y., Hoose, C., Korolev, A., Kumjian, M. R., Milbrandt, J. A., Pawlowska, H., Posselt, D. J., Prat, O. P., Reimel, K. J., Shima, S.-I., van Diedenhoven, B., and Xue, L.: Confronting the challenge of modeling cloud and precipitation microphysics, J. Adv. Model. Earth Syst., 12, e2019MS001689, https://doi.org/10.1029/2019MS001689, 2020.

Noda, A. and Niino, H.: Critical grid size for simulating convective storms: A case study of the Del City supercell storm, Geophys. Res. Lett., 30, 2003.

Omanovic, N., Ferrachat, S., Fuchs, C., Henneberger, J., Miller, A. J., Ohneiser, K., and Lohmann, U.: Evaluating the Wegener–Bergeron–Findeisen process in ICON in large-eddy mode with in situ observations from the CLOUDLAB project, Atmos. Chem. Phys., 24, 6825–6844, https://doi.org/10.5194/acp-24-6825-2024,2024.

Papaevangelou, N., Villanueva, D., Eirund, G. K., Chen, J., Dedekind, Z., and Lohmann, U.: Simulations of selective seeding of hailstorms—A summertime case study over Switzerland, J. Appl. Meteorol. Climatol., 64, 1509–1524, 2025.

Papaevangelou, N., Villanueva, D., and Lohmann, U.: Impact of cloud seeding on simulated hailstorms and its dependence on CAPE, wind shear, and tracking thresholds, EGUsphere [preprint], https://doi.org/10.5194/egusphere-2025-6348, 2026.

Rauber, R. M., Geerts, B., Xue, L., French, J., Friedrich, K., Rasmussen, R. M., Tessendorf, S. A., Blestrud, D. R., Kunkel, M. L., and Parkinson, S.: Wintertime orographic cloud seeding: a review, J. Appl. Meteorol. Climatol., 58, 2117–2140, https://doi.org/10.1175/JAMC-D-18-0341.1, 2019.

Ray, P. S., Johnson, L. R., Priegnitz, D. L., Boe, B. A., and Mielke, P. W.: The morphology of several tornadic storms on 20 May 1977, J. Atmos. Sci., 38, 1643–1663, 1981.

Republic Hydrometeorological Service of Serbia, Hail Suppression Center: Instruction 5/2023: Methods for radar identification and seeding of single-cell, multicell, and supercell hail-producing storms using the OGIS automated system, Belgrade, Serbia, 2023.

Rudolph, R., Sackiw, C., and Riely, G.: Statistical evaluation of the 1984–88 seeding experiment in northern Greece, J. Weather Modif., 26, 53–60, 1994.

Schaefer, V. J.: The production of ice crystals in a cloud of supercooled water droplets, Science, 104, 457–459, https://doi.org/10.1126/science.104.2707.457, 1946.

Simeonov, P.: An overview of crop hail damage and evaluation of hail suppression efficiency in Bulgaria, J. Appl. Meteor., 35, 1574–1581, https://doi.org/10.1175/1520-0450(1996)035<1574:AOOCHD>2.0.CO;2, 1996.

Smith, P. L., Johnson, L. R., Priegnitz, D. L., Boe, B. A., and Mielke, P. W.: An exploratory analysis of crop hail insurance data for evidence of cloud seeding effects in North Dakota, J. Appl. Meteor., 36, 463–473, https://doi.org/10.1175/1520-0450(1997)036<0463:AEAOCH>2.0.CO;2, 1997.

Straka, J. M.: Cloud and Precipitation Microphysics, Cambridge University Press, 407 pp., 2009.

Ursu, A., Istrate, V., Jitariu, V., and Lazăr, I. L.: Hail damage detection: Integrating Sentinel-2 images with weather radar hail kinetic energy, Remote Sens., 17, 3850, https://doi.org/10.3390/rs17233850, 2025.

Vonnegut, B.: The nucleation of ice formation by silver iodide, J. Appl. Phys., 18, 593–595, https://doi.org/10.1063/1.1697813, 1947.

Vučković, V.: Numerical simulation of seeding of convective clouds, Doctoral thesis, University of Belgrade, Faculty of Physics, Department of Meteorology, 108 pp. (In Serbian), 2003.

Vučković, V., Vujović, D., and Jovanović, A.: Aerosol parameterisation in a three-moment microphysical scheme: Numerical simulation of submicron-sized aerosol scavenging, Atmos. Res., 273, 106148, https://doi.org/10.1016/j.atmosres.2022.106148, 2022.

Vučković, V., Vujović, D., and Savić, D.: Influence of electrostatic collection on scavenging of submicron-sized aerosols by cloud droplets and raindrops, Aerosol Sci. Technol., 57, 1154–1173, https://doi.org/10.1080/02786826.2023.2251551, 2023.

Vučković, V., Vujović, D., Savić, D., and Filipović, L.: Impact of electro-collection and ice nucleation on aerosol scavenging, Aerosol Sci. Technol., 59, 1006–1026, 2025a.

Vučković, V., Vujović, D., Savić, D., and Filipović, L.: The effect of electrocollection by ice hydrometeors on the scavenging of submicron-sized aerosol particles, Atmosphere, 16, 1265, https://doi.org/10.3390/atmos16111265, 2025b.

Vujović, D., Vučinić, Z., and Babić, Z.: 40 Years of Hail Suppression in Serbia, 9th WMO Scientific Conference on Weather Modification and Weather Modification Workshop, Antalya, Turkey, No. 1406, 2007.

Wang, X., Zhang, L., and Moran, M. D.: Uncertainty assessment of current size-resolved parameterizations for below-cloud particle scavenging by rain, Atmos. Chem. Phys., 10, 5685–5705, 2010.

World Meteorological Organization: WMO statement on weather modification, https://wmo.int/content/wmo-statement-weather-modification, last access: 4 March 2026, 2025.

Xue, M., Droegemeier, K. K., and Wong, V.: The Advanced Regional Prediction System (ARPS)—A multiscale nonhydrostatic atmospheric simulation and prediction tool. Part I: Model dynamics and verification, Meteorol. Atmos. Phys., 75, 161–193, 2000.

Xue, M., Droegemeier, K. K., Wong, V., Shapiro, A., Brewster, K., Carr, F., Weber, D., Liu, Y., and Wang, D.: The Advanced Regional Prediction System (ARPS)—Part II: Model physics and applications, Meteorol. Atmos. Phys., 76, 143–165, 2001.

Xue, L., Hashimoto, A., Murakami, M., Rasmussen, R., Tessendorf, S. A., Breed, D., Parkinson, S., Holbrook, P., and Blestrud, D.: Implementation of a silver iodide cloud-seeding parameterization in WRF. Part I: Model description and idealized 2D sensitivity tests, J. Appl. Meteorol. Climatol., 52, 1433–1457, https://doi.org/10.1175/JAMC-D-12-0148.1, 2013a.

875 Xue, L., Tessendorf, S. A., Nelson, E., Rasmussen, R., Breed, D., Parkinson, S., Holbrook, P., and Blestrud, D.: Implementation of a silver iodide cloud-seeding parameterization in WRF. Part II: 3D simulations of actual seeding events and sensitivity tests, J. Appl. Meteorol. Climatol., 52, 1458–1476, https://doi.org/10.1175/JAMC-D-12-0149.1, 2013b.

Zalesak, S. T.: Fully multidimensional flux-corrected transport algorithms for fluids, J. Comput. Phys., 31, 335–362, 1979.

880 Zhang, L., Wang, X., Moran, M. D., and Feng, J.: Review and uncertainty assessment of size-resolved scavenging coefficient formulations for below-cloud snow scavenging of atmospheric aerosols, Atmos. Chem. Phys., 13, 10005–10025, 2013.

Young, K. C.: Microphysical processes in clouds, Oxford University Press, New York, 427 pp., 1993.